

# Journal Pre-proof



Characterization of SARS-CoV-2 N protein reveals multiple functional consequences of the C-terminal domain

Chao Wu, Abraham J. Qavi, Asmaa Hachim, Niloufar Kavian, Aidan R. Cole, Austin B. Moyle, Nicole D. Wagner, Joyce Sweeney-Gibbons, Henry W. Rohrs, Michael L. Gross, J. S. Malik Peiris, Christopher F. Basler, Christopher W. Farnsworth, Sophie A. Valkenburg, Gaya K. Amarasinghe, Daisy W. Leung

PII: S2589-0042(21)00649-0

DOI: <https://doi.org/10.1016/j.isci.2021.102681>

Reference: ISCI 102681

To appear in: *ISCIENCE*

Received Date: 16 December 2020

Revised Date: 13 May 2021

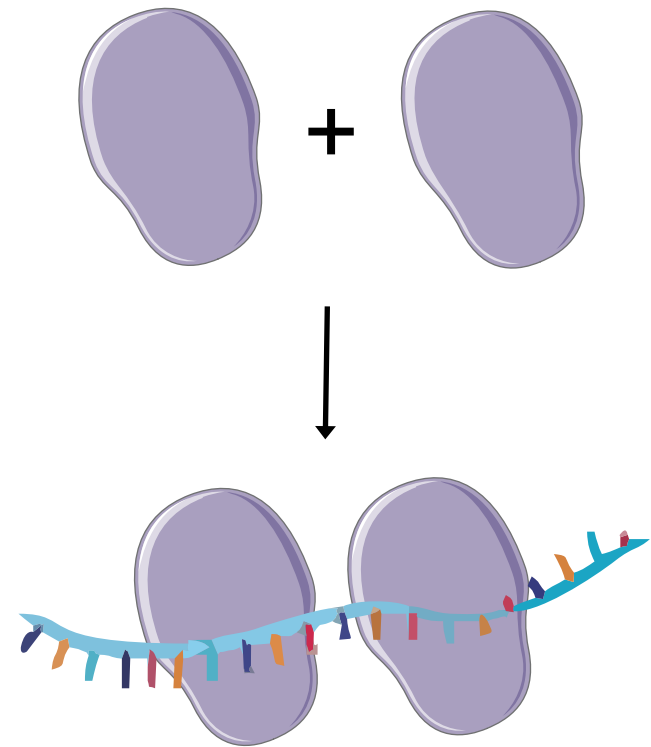
Accepted Date: 28 May 2021

Please cite this article as: Wu, C., Qavi, A.J., Hachim, A., Kavian, N., Cole, A.R., Moyle, A.B., Wagner, N.D., Sweeney-Gibbons, J., Rohrs, H.W., Gross, M.L., Peiris, J.S.M., Basler, C.F., Farnsworth, C.W., Valkenburg, S.A., Amarasinghe, G.K., Leung, D.W., Characterization of SARS-CoV-2 N protein reveals multiple functional consequences of the C-terminal domain, *ISCIENCE* (2021), doi: <https://doi.org/10.1016/j.isci.2021.102681>.

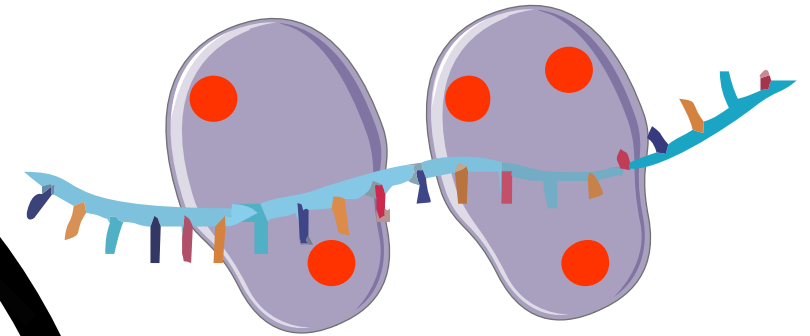
This is a PDF file of an article that has undergone enhancements after acceptance, such as the addition of a cover page and metadata, and formatting for readability, but it is not yet the definitive version of record. This version will undergo additional copyediting, typesetting and review before it is published in its final form, but we are providing this version to give early visibility of the article. Please note that, during the production process, errors may be discovered which could affect the content, and all legal disclaimers that apply to the journal pertain.

© 2021

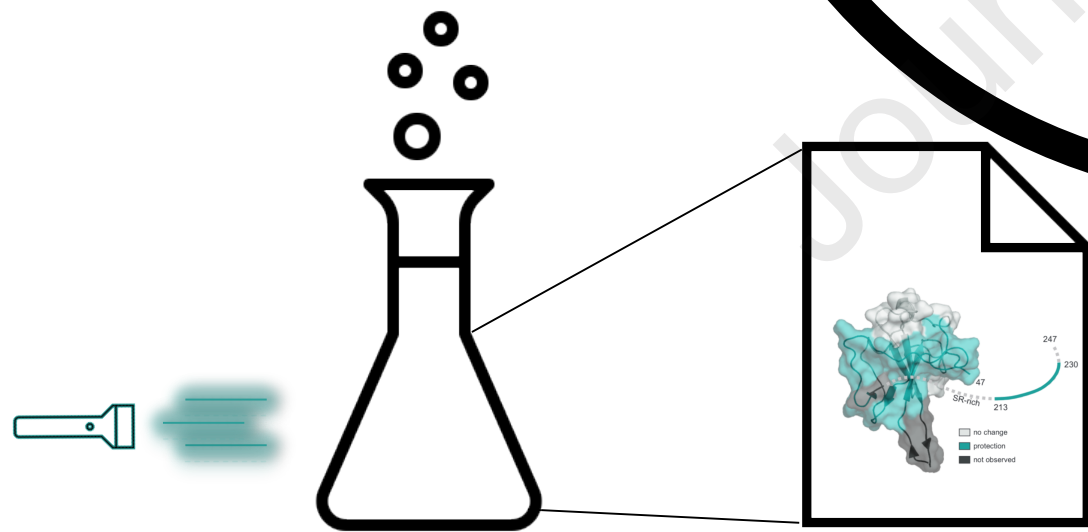
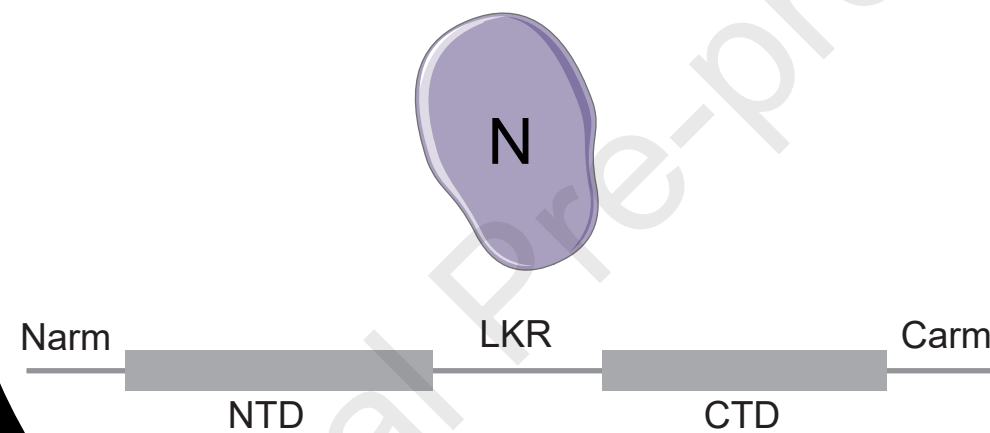
① Oligomerization provides a high affinity RNA binding platform



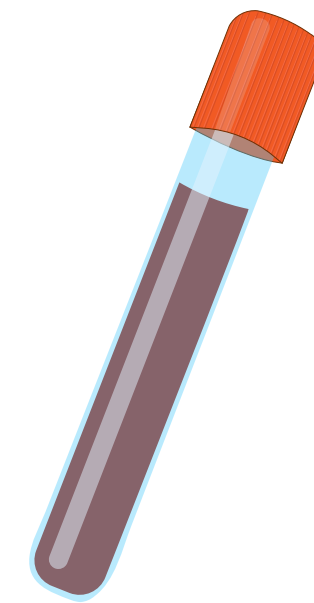
③ Phosphoregulation:  
reduced RNA affinity  
N-RNA morphological changes



SARS-CoV-2 Nucleocapsid (N)



② RNA binding interface mapping



④ Improved serological marker with CTD

# 1 **Characterization of SARS-CoV-2 N protein reveals multiple** 2 **functional consequences of the C-terminal domain**

3

4 Chao Wu<sup>1</sup>, Abraham J. Qavi<sup>1\*</sup>, Asmaa Hachim<sup>2\*</sup>, Niloufar Kavian<sup>2,3,4\*</sup>, Aidan R. Cole<sup>1\*</sup>,  
5 Austin B. Moyle<sup>6\*</sup>, Nicole D. Wagner<sup>6\*</sup>, Joyce Sweeney-Gibbons<sup>7\*</sup>, Henry W. Rohrs<sup>6</sup>,  
6 Michael L. Gross<sup>6</sup>, J. S. Malik Peiris<sup>2,8</sup>, Christopher F. Basler<sup>7</sup>, Christopher W.  
7 Farnsworth<sup>1#</sup>, Sophie A. Valkenburg<sup>2#</sup>, Gaya K. Amarasinghe<sup>#1Δ</sup>, and Daisy W.  
8 Leung<sup>1,5#</sup>,

9 <sup>1</sup>Department of Pathology and Immunology, Washington University School of Medicine in St.  
10 Louis, St. Louis, MO, USA.

11 <sup>2</sup>HKU-Pasteur Research Pole, School of Public Health, The University of Hong Kong, Hong  
12 Kong, China

13 <sup>3</sup>Université Paris Descartes, Sorbonne Paris Cité, Faculté de Médecine, Assistance Publique–  
14 Hôpitaux de Paris, Hôpital Universitaire Paris Centre, Centre Hospitalier Universitaire Cochin,  
15 Service d'Immunologie Biologique, Paris, France.

16 <sup>4</sup>Institut Cochin, INSERM U1016, Université Paris Descartes, Sorbonne Paris Cité, Paris,  
17 France

18 <sup>5</sup>Department of Internal Medicine, Washington University School of Medicine in St. Louis, St.  
19 Louis, MO, USA.

20 <sup>6</sup>Department of Chemistry, Washington University in St. Louis, St. Louis, MO, USA.

21 <sup>7</sup>Center for Microbial Pathogenesis, Institute for Biomedical Sciences, Georgia State University,  
22 Atlanta, GA, USA

23 <sup>8</sup>Division of Public Health Laboratory Sciences, School of Public Health, Li Ka Shing Faculty of  
24 Medicine, The University of Hong Kong, Hong Kong, China

25 \*equal contributions

26 #corresponding authors. Email addresses: [gamarasinghe@wustl.edu](mailto:gamarasinghe@wustl.edu), [dwleung@wustl.edu](mailto:dwleung@wustl.edu),  
27 [sophie.v@hku.hk](mailto:sophie.v@hku.hk), [cwfarnsworth@wustl.edu](mailto:cwfarnsworth@wustl.edu).

28 Δ lead author

29 Key words: SARS-CoV-2, COVID-19, phase separation, nucleoprotein, serology

30

**31 Summary**

32 Nucleocapsid (N) encoded by SARS-CoV-2 plays key roles in the replication cycle and  
33 is a critical serological marker. Here we characterize essential biochemical properties of  
34 N and describe the utility of these insights in serological studies. We define N domains  
35 important for oligomerization and RNA binding and show that N oligomerization  
36 provides a high affinity RNA binding platform. We also map the RNA binding interface,  
37 showing protection in the N-terminal domain and linker region. In addition,  
38 phosphorylation causes reduction of RNA binding and redistribution of N from liquid  
39 droplets to loose-coils, showing how N/RNA accessibility and assembly may be  
40 regulated by phosphorylation. Finally, we find that the C-terminal domain of N is the  
41 most immunogenic, based upon antibody binding to patient samples. Together, we  
42 provide a biochemical description of SARS-CoV-2 N and highlight the value of using N  
43 domains as highly specific and sensitive diagnostic markers.

44

45

46

47

48

49

50

51

## 52 Introduction

53 Severe acute respiratory syndrome coronavirus 2 (SARS-CoV-2) is a novel coronavirus  
54 and the causative agent of COVID-19. Coronavirus has a single-stranded, positive-  
55 sense RNA genome encoding for four major structural proteins: spike (S), envelope (E),  
56 membrane (M), and nucleocapsid (N). The N protein is the second most proximal to the  
57 3' end of the genome and is one of the most abundantly expressed viral proteins given  
58 the multifunctional roles of N during viral replication and assembly (Fung and Liu, 2019;  
59 Kim et al., 2020; McBride et al., 2014; Perlman and Netland, 2009). It is estimated that  
60 1,000 copies of N are incorporated into each virion compared to only 100 copies of S  
61 (Bar-On et al., 2020). N exists mostly in a phosphorylated state in the cytoplasm,  
62 whereas it is predominantly dephosphorylated in mature virions, suggesting that N  
63 function is regulated by phosphorylation (Wu et al., 2014; Wu et al., 2009).

64 A major function of N is to encapsidate the ssRNA viral genome to evade immune  
65 detection and to protect the viral RNA from degradation by host factors (Chang et al.,  
66 2014; McBride et al., 2014). N has two structural domains (**Figure 1A**): an N-terminal  
67 domain (NTD; amino acid residues 44-176) and a C-terminal domain (CTD; amino acid  
68 residues 248-369). NTD is generally referred to as the RNA-binding domain (RBD),  
69 although regions outside of NTD are implicated in RNA binding as well (Chang et al.,  
70 2014; Grosseohme et al., 2009; Gui et al., 2017; Kang et al., 2020; McBride et al., 2014).  
71 N<sub>CTD</sub> exists as a dimer in solution and can also bind RNA (Bouhaddou et al., 2020; Gui  
72 et al., 2017; Takeda et al., 2008). A conserved serine/arginine rich-linker region (LKR)  
73 connects the NTD and CTD (**Figure 1A** and **Supp. Figure 1A**) (Chang et al., 2014).  
74 Phosphorylation of residues in the serine-arginine of LKR is believed to regulate

75 discontinuous transcription, particularly for shorter subgenomic mRNA closer to the 3'  
76 end during early stages of replication (Wu et al., 2014; Wu et al., 2009). The LKR along  
77 with residues at the extreme N and C termini (Narm: amino acid residues 1-43 and  
78 Carm: amino acid residues 370-419) are intrinsically disordered (Chang et al., 2014;  
79 Cubuk et al., 2021). However, relative to the Narm and Carm, the LKR is more  
80 conserved (**Figure 1B** and **Supp. Figure 1B**).

81 Given its abundant expression and conservation within the genome, N has been used  
82 as an antigen for serology tests (Chew et al., 2020; Tang et al., 2020a, b). Previous  
83 studies showed that N-specific antibodies dominate the overall antibody response  
84 (Hachim et al., 2020; Lu et al., 2021). Furthermore, the T cell responses directed  
85 towards N are highly immunodominant in SARS-CoV and SARS-CoV-2 infection, with  
86 N-specific memory T cell responses evident 17 years after the initial SARS-CoV  
87 infection (Le Bert et al., 2020). Thus, N protein stability, RNA binding characteristics,  
88 abundance, and conservation are likely to impact T and B cell immunity.

89 Previous studies, including our own revealed shared and unique functions among viral  
90 nucleocapsid proteins (Arragain et al., 2019; Ding et al., 2016; Lu et al., 2020; Luo et al.,  
91 2020; Raymond et al., 2010; Su et al., 2018; Wan et al., 2017). These insights include  
92 oligomerization, RNA binding, and N-dependent functions such as RNA synthesis and  
93 immune evasion. Here we use a series of biochemical and biophysical assays to dissect  
94 different regions in N in order to determine how oligomerization, RNA binding, and  
95 phosphorylation are coupled to functions of N. Our results reveal that oligomeric N  
96 provides a continuous platform for binding RNA with high affinity. Our HDX-MS data  
97 identified a novel RNA binding region within the LKR in addition to a positively charged

98 patch within the NTD. We also show that phosphorylation modulates N-RNA  
99 interactions and solution properties, including phase-separated droplets. Finally, we find  
100 that the CTD contributes to oligomerization and RNA binding and is efficient at  
101 suppressing immune signaling. In SARS-CoV-2 infected patient plasma samples, the  
102 truncated CTD of N provides a highly sensitive serological marker. Our studies add to  
103 the wealth of information on SARS-CoV-2 N protein and expands upon our knowledge  
104 into N domain-specific functions.

105

## 106 **Results**

107 **Multiple regions within N protein contribute to oligomerization.** While several  
108 studies on SARS coronavirus N proteins report that N proteins oligomerize and that N  
109 oligomers is important for the assembly of viral particles (Chang et al., 2009; Luo et al.,  
110 2005; Ye et al., 2020), the contribution of each N domain to oligomerization remains to  
111 be defined. To better understand the regions within SARS-CoV-2 N important for  
112 promoting N-N interactions, we first used dynamic light scattering (DLS) to determine  
113 the hydrodynamic properties of isolated, RNA-free N domains and combinations of  
114 domains. Analysis of DLS results show that there are two major oligomeric species for  
115 full-length N ( $N_{WT}$ ; 46 kDa), with hydrodynamic radii ( $R_h$ ) of 8.9 nm and 450 nm (**Figure**  
116 **1C and 1D**), suggesting the presence of different oligomeric forms of the protein. For  
117 comparison, the  $R_h$  values for maltose binding protein (44 kDa) and bovine serum  
118 albumin (66 kDa) are 2.9 nm and 3.7 nm, respectively. Removal of the Narm and Carm  
119 ( $N_{NTD-LKR-CTD}$ ) results in two major species that are similar to  $N_{WT}$ . However, both  $N_{NTD-}$   
120  $LKR-CTD$  populations display reduced polydispersity (narrower peak width, **Supp. Figure**

121 **2A**), suggesting that both Narm and Carm contribute to N oligomerization. Further  
122 removal of the CTD ( $N_{\text{NTD-LKR}}$ ) results in a single peak representing a dimeric species  
123 ( $R_h = 3.9$  nm), but with considerable polydispersity.  $N_{\text{NTD}}$  and  $N_{\text{CTD}}$  alone form stable  
124 domains;  $N_{\text{NTD}}$  is a monomer ( $R_h = 2.3$  nm) whereas  $N_{\text{CTD}}$  is a dimer in solution ( $R_h =$   
125  $3.5$  nm), consistent with previous studies (Takeda et al., 2008). Exact mass  
126 measurement by denaturing mass spectrometry yields values corresponding to the  
127 mass expected from the amino acid sequence ( $\pm 1$  Da) and supports the identity of the  
128 constructs used here (**Supp. Figure 2B-E**).

129

130 **Oligomeric N provides a platform for high affinity RNA binding.** A critical function  
131 for N is to bind and encapsidate viral genomic ssRNA (Chang et al., 2014). This  
132 interaction is sequence independent and as a result of N-RNA interactions, newly  
133 synthesized viral RNA often avoid immune detection by cellular pattern recognition  
134 receptors (Leung and Amarasinghe, 2016). Previous results suggest that regions  
135 beyond the NTD are involved in RNA binding, but were limited by experimental  
136 detection and only select regions were characterized (Chang et al., 2009; Grosseohme  
137 et al., 2009; Keane et al., 2012). To address this limitation and to gain insight into how  
138 each domain of SARS-CoV-2 N contributes to RNA binding, we developed a sensitive  
139 fluorescence polarization (FP) assay to measure binding of a FITC-labeled 20-nt ssRNA  
140 (sequence: UUUCACCUCCCUUUCAGUUU) (**Figure 2A**). From this assay, we find that  
141  $N_{\text{WT}}$  binds the 20-nt ssRNA with high affinity ( $K_D = 0.007 \pm 0.001$   $\mu\text{M}$ ). Removal of the  
142 Narm and Carm do not impact ssRNA binding ( $K_D = 0.006 \pm 0.002$  and  $0.006 \pm 0.002$   
143  $\mu\text{M}$  for  $N_{\text{NTD-LKR-CTD-Carm}}$  and  $N_{\text{NTD-LKR-CTD}}$ , respectively) (**Figure 2B**). In contrast, the

144 isolated  $N_{\text{NTD}}$  and  $N_{\text{CTD}}$  have low affinity binding ( $K_D = 20 \pm 10$  and  $13 \pm 5 \mu\text{M}$ ,  
145 respectively). However, inclusion of the LKR region increased RNA binding affinity  
146 significantly ( $0.50 \pm 0.08$  and  $0.35 \pm 0.04 \mu\text{M}$  for  $N_{\text{NTD-LKR}}$  and  $N_{\text{LKR-CTD}}$ ) (**Figure 2B-2D**).  
147 Addition of CTD onto NTD-LKR *in cis* increases the binding affinity to the single digit nM  
148 range ( $0.006 \pm 0.002 \mu\text{M}$ ) (**Figure 2C**), but not *in trans* (compare  $N_{\text{NTD-LKR}} + N_{\text{CTD}}$  with  
149  $N_{\text{NTD-LKR-CTD}}$ ). The increase in binding affinity also occurs when NTD is added to LKR-  
150 CTD *in cis* (**Figure 2D**, compare  $N_{\text{LKR-CTD}} + N_{\text{NTD}}$  with  $N_{\text{NTD-LKR-CTD}}$ ). Similar binding  
151 curves and  $K_D$  values were obtained when fluorescence anisotropy values were  
152 converted from polarization (**Supp. Figure 3A**). Collectively, our data quantitatively  
153 show that the NTD, CTD, and LKR each contribute to ssRNA binding and that the  
154 presence of these three domains in tandem confers N with high affinity RNA binding,  
155 suggesting a more extensive and coupled RNA binding interface on N than is  
156 encompassed within a single domain.

157

158 N is proposed to disrupt dsRNA structures formed by transcription regulatory sequences  
159 during discontinuous transcription and impact viral RNA synthesis (Grossoehme et al.,  
160 2009; Keane et al., 2012; Sola et al., 2015). In order to evaluate the impact of N binding  
161 to dsRNA structures, we used an RNA that forms a stable stem-loop structure (sIRNA)  
162 (sequence: GGAAGAUUAAUAAUUUCC) (**Figure 2E**). We find that  $N_{\text{WT}}$  binds this  
163 sIRNA with relative high affinity ( $K_D = 0.051 \pm 0.004 \mu\text{M}$ ) whereas both  $N_{\text{NTD}}$  and  $N_{\text{CTD}}$   
164 alone have significantly weaker binding affinities ( $K_D = 120 \pm 80$  and  $60 \pm 40 \mu\text{M}$ ,  
165 respectively). Addition of LKR significantly improves binding, consistent with results  
166 observed for ssRNA. Overall, sIRNA binding to N appears to be at an order of

167 magnitude lower than to ssRNA binding (**Supp. Figure 3B**). This is potentially due, in  
168 part, to the energetic penalty of unfolding the stem-loop structure. Furthermore, the  
169 Narm and Carm may contribute more to siRNA binding than ssRNA because the impact  
170 on N binding is more pronounced after removal of the Narm or Carm (**Supp. Figure 3C**).

171

172 **Hydrogen-deuterium exchange mass spectrometry (HDX-MS) defines an extended**  
173 **RNA binding interface in N.** X-ray crystal and NMR structures are available for the  
174 SARS-CoV-2 N<sub>NTD</sub> and N<sub>CTD</sub> as well as hybrid models for RNA-bound N<sub>NTD</sub> (Dinesh et  
175 al., 2020b; Kang et al., 2020; Ye et al., 2020). While these static structures provide a  
176 wealth of information, a critical gap remains in our knowledge of N-RNA interactions.  
177 Our studies here show that other N domains *in cis* contribute significantly to RNA  
178 binding. To further define the RNA binding interface on N, we performed HDX-MS to  
179 locate regions that become protected upon RNA binding. We first tested the N<sub>NTD-LKR-CTD</sub>  
180 protein, but observed aggregation upon RNA binding that caused a 100-fold loss in  
181 peptide abundances for the bound state, possibly attributable to aggregation-induced  
182 poor digestion. To circumvent RNA-binding induced protein aggregation, we reasoned  
183 that shorter constructs, such as N<sub>NTD-LKR</sub>, could be used based on our binding studies.  
184 However, even for this shorter construct, we noticed that the sample became cloudy  
185 after mixing with RNA. Next, given phosphorylation of N is a crucial regulatory  
186 mechanism in the coronavirus life cycle (Wu et al., 2009), we hypothesized that N  
187 phosphorylation likely impacts N-RNA solution properties and stability. Therefore, we  
188 examined phosphomimics of N for improved sample stability and solubility that are  
189 compatible with HDX-MS studies. For SARS-CoV, glycogen synthase kinase (GSK)-3

190 was shown to phosphorylate N at Ser177 (corresponding to Ser176 in SARS-CoV-2 N)  
191 (Wu et al., 2009). Phosphorylation of Ser177 is preceded by phosphorylation of Ser189  
192 and Ser207 (Ser188 and 206 in SARS-CoV-2 N) by priming kinases (Wu et al., 2009).  
193 While more phosphorylation events may occur, we focused on these three better-known  
194 positions to evaluate if introduction of S176D/S188D/S206D mutations into N<sub>NTD-LKR</sub>  
195 (N<sub>NTD-LKR S176D/S188D/S206D</sub>) will resolve N protein aggregation at the concentrations of  
196 interest.

197 With the introduction of the mutations on a shorter construct, N<sub>NTD-LKR S176D/S188D/S206D</sub>,  
198 we were able to use sequential FXIII and pepsin digestion to recover 152 peptides,  
199 resulting in 93.3% sequence coverage (**Supp. Figure 4**), which enabled us to further  
200 examine the system by HDX-MS. HDX-MS analysis of N<sub>NTD-LKR S176D/S188D/S206D</sub> shows  
201 clear protection in four distinct regions upon RNA binding (amino acid residues 41-63,  
202 105-108, 146-171, and 213-230) (**Figure 3A-B** and **Mendeley dataset**  
203 doi:10.17632/sv8r6phkzt.1). Residues 133-143 are not perturbed by RNA binding, but  
204 peptides covering residues 146-171 show clear protection. The largest differences in  
205 HDX are observed where 50-80% of the residues of unbound peptides undergo a burst  
206 phase of HDX in the first 10 s (amino acid residues 146-156, 163-171, and 213-230),  
207 where the peptides cover regions of little hydrogen bonding in the unbound state. When  
208 bound to RNA, the fraction of residues participating in the burst phase decreases,  
209 resulting in observed protection. Then, HDX either converges over time (amino acid  
210 residues 146-156, 163-171, and 219-223) consistent with protein conformation or RNA  
211 binding dynamics, or the HDX never converges in the timescale of the experiment  
212 (amino acid residues 222-230), consistent with relatively static binding. Interestingly,

213 peptides covering amino acid residues 103-108 and 156-159 undergo very little HDX  
214 throughout the experiment, consistent with either a hydrophobic pocket or secondary or  
215 tertiary structure hydrogen bonding. Of note, HDX decreases for the bound state in  
216 these peptides only after 1 h. The low initial HDX limits the dynamic range of binding-  
217 induced protection from HDX, but statistically significant protection is still observed.

218 Overall, HDX analysis revealed that the protected regions (**Figure 3C**) overlap with a  
219 basic patch groove in the N<sub>NTD</sub> structure (**Figure 3D**) that is also observed in recently  
220 published NMR titration studies (Dinesh et al., 2020a); however, a region (amino acid  
221 residues 213-230) within the LKR domain, C-terminal to the SR-motif, also shows  
222 statistically significant HDX protection. This observation is consistent with the C-terminal  
223 end of the LKR domain, a region truncated in other RNA-binding studies of similar N  
224 proteins, being perturbed by RNA binding; furthermore, the parallel HDX kinetics plots  
225 indicate relatively static binding interactions within this region. Interestingly, we did not  
226 detect HDX protection in the SR-motif, which was proposed to bind RNA. This may be  
227 due to the Ser-to-Asp mutations introduced into this region, changing the RNA binding  
228 patterns. Altogether, HDX results along with our biochemical data define an RNA-  
229 binding interface within the NTD and LKR regions of N.

230

231 **N-RNA liquid droplet formation is impacted by N domains.** The above  
232 oligomerization and RNA binding results were obtained using RNA-free protein.  
233 However, oligomerization is an intrinsic property of N and is complicated by RNA  
234 binding during copurification due to the high affinity of N proteins for RNA. We found  
235 that bacterial RNA copurified even with increased ionic strength in purification buffer.

236 Size exclusion chromatography revealed three populations of N, including two RNA-  
237 bound states (p1 and p2) and an RNA-free state (p3) (**Figure 4A**). Truncation of the  
238 Narm results in an increase of the RNA-free peak (p3), suggesting that N truncations  
239 can alter the structure of N and correspondingly impact RNA binding and  
240 oligomerization. When both Narm and Carm were removed, we observed an even  
241 greater shift to p3, suggesting that both arms contribute to RNA binding interactions. To  
242 gain a better understanding of the two RNA-bound populations p1 and p2, we visualized  
243 these samples by using negative-stain electron microscopy (EM) in near-physiological  
244 salt concentrations (150 mM). We observed that N<sub>WT</sub> p1 contains N-RNA with a loose-  
245 coil appearance (**Figure 4B, top left**), similar to that observed for other RNA-bound  
246 nucleocapsids (Bharat et al., 2012; Mavrakis et al., 2002). In contrast, we mostly  
247 observe spheres in N<sub>WT</sub> p2 that correspond to liquid droplets separated from the  
248 surrounding buffer (**Figure 4B, top right**), consistent with many recent studies that  
249 describe liquid-liquid phase separation (LLPS) of N in the presence of RNA (Carlson et  
250 al., 2020; Cubuk et al., 2021; Iserman et al., 2020; Jack et al., 2020; Savastano et al.,  
251 2020).

252

253 To determine if N regions that impact RNA binding also impact liquid droplet formation,  
254 we next examined the role of Narm and Carm. N<sub>NTD-LKR-CTD-Carm</sub> behaves similarly to N<sub>WT</sub>,  
255 having loose-coils in p1 (**Figure 4B, middle left**) and forming spherical liquid droplets in  
256 p2 (**Figure 4B, middle right**). However, examination of p2 from N<sub>NTD-LKR-CTD</sub> (**Figure 4B,**  
257 **bottom right**) revealed a much smaller population of liquid droplets (red arrow) and  
258 mostly crystal-like needle aggregates, suggesting that the Carm is important for droplet

259 formation. A transition from spherical liquids to needle-like solids is consistent with the  
260 liquid-to-solid transitions observed for other proteins that undergo phase separation  
261 (Patel et al., 2015).

262

### 263 **Phosphorylation of LKR modulates RNA binding and higher-order assembly.**

264 Recently N protein phosphorylation has been qualitatively shown to modulate both RNA  
265 binding and phase separation (Carlson et al., 2020; Lu et al., 2020; Savastano et al.,  
266 2020), and we successfully utilized the improved solubility of phosphomimics to map the  
267 RNA binding interface within the NTD-LKR region. To further test how phosphorylation  
268 quantitatively impacts RNA binding and solution properties of SARS-CoV-2 N-RNA, we  
269 generated additional N phosphomimics in the context of N<sub>WT</sub> and N<sub>NTD-LKR</sub>. Size  
270 exclusion chromatography showed that, compared to N<sub>WT</sub>, N<sub>S188D/S206D</sub> (priming serine  
271 residues for S176 by GSK-3) produced a reduced RNA-free peak (p3) and an increased  
272 RNA-bound peak (p1) (**Figure 4C**). Introduction of S176D to generate N<sub>S176D/S188D/S206D</sub>  
273 resulted in an even greater shift in p1 and p3 distributions, showing how  
274 phosphorylation can affect N interactions with RNA. The height of p2 remains relatively  
275 the same for all preparations. Examination of these protein peaks using electron  
276 microscopy revealed that N<sub>S188D/S206D</sub> displays similar loose-coils in p1 (**Figure 4D, top**  
277 **left**) and spherical droplets in p2 (**Figure 4D, top right**) for the RNA-bound species.  
278 Similar observations were made for N<sub>S176D/S188D/S206D</sub> (**Figure 4D**). To describe this  
279 interaction further, we measured ssRNA binding to the N phosphomimics (**Figure 4E**  
280 and **Supp. Figure 5A**). N<sub>S176D/S188D/S206D</sub> displays ~5-fold lower binding affinity to ssRNA  
281 compared to N<sub>WT</sub> binding, a result in trend with previous work examining the impact of

282 LKR phosphorylation on RNA binding through simulations (Savastano et al., 2020). We  
283 observed a similar trend of lower binding to phosphomimics for the N<sub>NTD-LKR</sub> construct.  
284 Furthermore, binding to siRNA is also affected by these mutations (**Supp. Figure 5B**).  
285 Collectively, our data suggest that phosphorylation of the LKR region can impact N  
286 interactions with RNA, causing changes in properties, including solvent accessibility and  
287 RNA binding. Interestingly, there are 14 serine residues in the SR motif of LKR in  
288 SARS-CoV-2 N, of which 13 are found in SARS-CoV N, and an increase in  
289 phosphorylation in this region may further enhance these changes for RNA interaction  
290 and N associated functions.

291

292 **N<sub>CTD</sub> is a sensitive serological marker.** Given that the different domains of N impact  
293 the various biochemical and physicochemical properties of N, we next assessed if  
294 particular domains contribute more significantly to N immunodominance that has been  
295 observed worldwide (Hachim et al., 2020). We also asked if there is a correlation  
296 between the biophysical properties, including RNA binding by N, and domain-specific  
297 responses in COVID-19 patient responses. Plasma samples collected from two cohorts  
298 of RT-PCR confirmed COVID-19 patients, one in St. Louis, USA (n = 45) and one in  
299 Hong Kong (n = 23), at different time points of infection. Using these samples, we  
300 performed enzyme-linked immunosorbent assays (ELISAs) to detect IgG present in  
301 COVID-19 patient plasma using different N domains that we have purified and  
302 characterized. First, we confirmed that purified N<sub>WT</sub> is a sensitive serological marker to  
303 differentiate between COVID-19 positive and negative individuals (**Figure 5A**). As  
304 shown in **Figure 5B**, antibodies against all five N constructs were detected in the

305 COVID-19 cohort ( $p < 0.0001$  versus negative controls for all). A cut-off based on the  
306 mean of the negatives plus three standard deviations allowed us to assess the  
307 performance of each N construct at detecting IgG antibodies in COVID-19 positive  
308 individuals (**Figure 5C**). We find that  $N_{\text{NTD-LKR-CTD-Carm}}$  shows the lowest sensitivity  
309 (41.2%), whereas the truncated  $N_{\text{NTD-LKR-CTD}}$  can detect more COVID-19 positive  
310 individuals (70.6%). Furthermore,  $N_{\text{CTD}}$  shows the highest combination of sensitivity  
311 (75%) and specificity (96.4%) over the other N constructs tested. This is demonstrated  
312 by the lowest cut-off score for the  $N_{\text{CTD}}$  for negative control samples, despite a  
313 comparable level of amino acid sequence conservation of the  $N_{\text{CTD}}$  (29-41%) to the  
314  $N_{\text{NTD}}$  (32-48%) and  $N_{\text{LKR}}$  (28-42%) domains with common cold corona viruses (**Figure**  
315 **1B**).

316 We next compared the immunogenicity of  $N_{\text{NTD-LKR-CTD-Carm}}$  to  $N_{\text{CTD}}$  and  $N_{\text{NTD}}$  on an IgG  
317 heatmap during natural infection to an independent panel of 67 COVID-19 samples from  
318 Hong Kong. The magnitude of the IgG response to the  $N_{\text{NTD-LKR-CTD-Carm}}$  tends to follow  
319 the same trend as that of  $N_{\text{CTD}}$  (**Figure 5D**). When we assessed the kinetics of  $N_{\text{CTD}}$  and  
320 the  $N_{\text{NTD-LKR-CTD-Carm}}$  responses, we find that the magnitude of the  $N_{\text{CTD}}$  IgG detection  
321 tends to reach a similar level to that of  $N_{\text{NTD-LKR-CTD-Carm}}$  at convalescent time-points  
322 (after day 14) (**Figure 5E**). The ELISA ratio of  $N_{\text{CTD}}/N_{\text{NTD-LKR-CTD-Carm}}$  demonstrates this  
323 finding, pointing to a maturation of the humoral immune response towards the  $N_{\text{CTD}}$  with  
324 time after infection (**Figure 5F**,  $p < 0.0001$  for acute versus convalescent time-points).  
325 The early dominance of the  $N_{\text{NTD-LKR-CTD-Carm}}$  IgG response may reflect the recruitment of  
326 a cross-reactive pre-existing N-specific response. This response becomes more specific  
327 with time for the  $N_{\text{CTD}}$  domain as a *de novo* antibody response is made.

328

329 Given that some RNA viral N proteins are known immune antagonists, including prior  
330 studies of SARS-CoV, we hypothesized that N from SARS-CoV-2 may also suppress  
331 the type-I interferon (IFN) signaling pathway (Messaoudi et al., 2015). Using an IFN $\beta$   
332 promoter reporter assay, we showed that N has a role in suppressing IFN signaling  
333 pathway when stimulated by Sendai virus (SeV) infection (**Figure 5G**). N<sub>WT</sub> can inhibit  
334 IFN $\beta$  promoter activity, although not as well as M $\ddot{e}$ ngl $\grave{a}$  virus (MLAV) VP35, a potent  
335 inhibitor of IFN signaling (Williams et al., 2020). Both N<sub>Narm-NTD-LKR</sub> and N<sub>NTD</sub> show  
336 modest inhibition at the highest concentration tested. However, N<sub>CTD-Carm</sub> shows similar  
337 levels of inhibition as N<sub>WT</sub>, and N<sub>CTD</sub> displays the highest inhibition even at lower  
338 concentrations. In summary, N is a potent inhibitor of IFN signaling and the N<sub>CTD</sub>  
339 appears to be the region critical for mediating this function.

340

## 341 Discussion

342 SARS-CoV-2 N protein is a core viral protein produced by the subgenomic RNA,  
343 positioned proximal to the 3' end of genome, displays high transcription levels, and is in  
344 high abundance in virions. N is prone to forming higher-order oligomers that is impacted  
345 by the presence of different domains. We found that the isolated N<sub>NTD</sub> and N<sub>CTD</sub> form  
346 well-behaved monomers and dimers, respectively. Linkage of the two domains through  
347 the LKR and addition of the Narm and Carm contribute to N oligomerization,  
348 demonstrated in our DLS studies. It also contributes to enhancement of RNA binding to  
349 a continuous platform that were quantitatively measured using a sensitive fluorescence

350 polarization assay. Using HDX-MS for the N<sub>NTD-LKR</sub> phosphomimic, we confirmed a  
351 major positively charged groove as an RNA binding region in the N<sub>NTD</sub> but also revealed  
352 that unstructured regions flanking the SR motif in the LKR are important for RNA  
353 interactions, which was not included in previous studies and crystal structures. The high  
354 extent of HDX observed for the LKR domain in the absence of RNA is consistent with  
355 minimal hydrogen bonding (i.e. minimal defined structure) and thus with a lack of  
356 structural information from other techniques; RNA-induced decreased HDX in the LKR  
357 domain could indicate RNA binding-induced secondary or tertiary structure, direct  
358 interactions with the RNA, or oligomerization. Overall, these results demonstrate the  
359 functional importance of the LKR domain for oligomerization and RNA binding. Thus,  
360 the coupling of oligomerization and RNA binding likely provides multilayered regulation  
361 that are important for immune evasion, viral replication, and nucleocapsid assembly.

362

363 N is also regulated by post-translational modifications and phosphorylation appears to  
364 play an important role that modulates RNA binding and changes the physicochemical  
365 properties of N. Our data revealed that mutation of S176, S188, and S206 in the SR  
366 motif to generate N phosphomimics resulted in decreased binding to RNA and a shift in  
367 protein-RNA populations with different solution properties.

368

369 In addition to characterizing the domain-specific biochemical and biophysical properties  
370 of N, we also gained insight into the antigenicity of individual domains of N and their  
371 potential utility in serological studies. Our data reveal that N<sub>CTD</sub> acts more specifically in

372 detecting infection of SARS-CoV-2, from patient plasma in comparison to N<sub>WT</sub>,  
373 consistent with predictions that the N<sub>CTD</sub> region encompasses major antigenic sites of N  
374 (Bussmann et al., 2006; Liang et al., 2005). Interestingly, 2 out of 10 individuals  
375 assessed in this study of longitudinal donors unexposed to SARS-CoV-2 by Edridge *et*  
376 *al.*, produced broadly reactive antibodies towards SARS-CoV-2 N<sub>WT</sub>. The possibility of  
377 broadly reactive antibodies in unexposed individuals highlights the need for domain-  
378 specific serology, such as our use of the N<sub>CTD</sub> for increased sensitivity to discriminate  
379 COVID-19 cases, while reducing the false-positive rate from cross-reactive antibodies  
380 generated by infections of the common-cold coronaviruses. Current sero-diagnostic  
381 assays to identify COVID-19 positive individuals are based on the detection of  
382 antibodies against N due to its abundant expression and corresponding high immune  
383 response (Chew et al., 2020; Tang et al., 2020a, b). However, these N-directed  
384 serological assays are highly variable, and their sensitivity depend on the sampling  
385 time-points, ranging from 0% to 93.75% (Liu et al., 2020; Tang et al., 2020a, b),  
386 suggesting that serological markers for SARS-CoV-2 infection can be further improved  
387 to include the N<sub>CTD</sub>.

388

389 In conclusion, we describe our efforts to characterize how different domains contribute  
390 to the biochemical and physicochemical properties of SARS-CoV-2 N. Our results  
391 advance the understanding of the different levels of regulation involved in modulating  
392 viral replication and highlight the utility of using the N<sub>CTD</sub> as a highly specific and  
393 sensitive diagnostic marker of COVID-19.

394

**395 Limitations of the study**

396 This study describes domain-specific insights into oligomerization, RNA binding, and  
397 phosphorylation of SARS-CoV-2 N protein. Generated reagents were then used to  
398 demonstrate that N<sub>CTD</sub> is a more sensitive and specific serology marker. However, the  
399 underlying mechanisms of how these biochemical properties contribute to the observed  
400 immunodominance of the CTD of N are not clear and warrant further studies.

401

**402 RESOURCE AVAILABILITY****403 Lead Contact**

404 Further information and requests for resources and reagents should be directed to and  
405 will be fulfilled by the lead contact, Gaya Amarasinghe (gamarasinghe@wustl.edu).

**406 Materials Availability**

407 Plasmids in this study are available with a completed Materials Transfer Agreement  
408 Request for these reagents by submitting to Dr. Gaya Amarasinghe  
409 (gamarasinghe@wustl.edu).

**410 Data and Code Availability**

411 HDX-MS peptides table and all kinetic plots are accessible in Mendeley  
412 (doi:10.17632/sv8r6phkzt.1).

413

**414 STAR Methods****415 EXPERIMENTAL MODEL AND SUBJECT DETAILS**

416 **Human Plasma.** The collection of patient plasma was approved by the Human  
417 Research Protection Office at Washington University in St. Louis (IRB reference number  
418 202007097) and the Institutional Review Board of The Hong Kong University and the  
419 Hong Kong Island West Cluster of Hospitals (IRB reference number UW20-169).

420

## 421 **METHOD DETAILS**

422 **Patients and sample collection.** Our study enrolled a total of 67 patients with RT-PCR  
423 confirmed COVID-19 infection: with 45 patients from St. Louis, MO, USA, and 23  
424 patients from Hong Kong, PRC. The negative samples (n = 28) used in this study were  
425 from St. Louis, USA, and were obtained from patients following the start of the  
426 pandemic. Plasma samples were obtained from patients at Barnes-Jewish Hospital (St.  
427 Louis, MO, USA) and the Hong Kong Island West Cluster of Hospitals (Hong Kong,  
428 PRC). Both hospital systems are urban, tertiary-care, academic medical centers.  
429 Positive and negative patients from all cohorts were confirmed using standard of care,  
430 RT-PCR based methods. Plasma samples were collected from heparinized blood.  
431 Sample day was defined as days post-symptom onset.

432

433 **Enzyme-linked immunosorbent assay (ELISA).** ELISA assays were performed with N  
434 proteins made in house, as described below. Briefly, recombinant N proteins were  
435 coated on 96 well flat bottom immunosorbent plates (Nunc Immuno MaxiSorp) at a  
436 concentration of 500 ng/mL, in 100  $\mu$ L coating buffer (PBS with 53%  $\text{Na}_2\text{CO}_3$  and 42%  
437  $\text{NaHCO}_3$ , pH 9.6) at 4°C overnight. An additional plate coated with a non-specific

438 protein (blocking buffer, PBS with 5% fetal bovine serum (FBS)) was used to measure  
439 the background binding of each plasma sample. Following FBS blocking and thorough  
440 washing, diluted plasma samples (1:100) were bound for 2 hours, further washed, and  
441 then detected by an anti-human IgG secondary antibody labelled with HRP (Invitrogen),  
442 and absorbance detected at 450 nm on a spectrophotometer (Wallac).

443  
444 **Protein Expression and Purification.** SARS-CoV-2 N constructs were expressed as  
445 His-tag fusion proteins in BL21 (DE3) *E. coli* cells (Novagen). At OD<sub>600</sub> of 0.6-0.7,  
446 recombinant protein expression was induced with 0.5 mM isopropyl β-d-1-  
447 thiogalactopyranoside (IPTG) for 12-14 h at 18°C. Cells were harvested and  
448 resuspended in lysis buffer containing 20 mM Tris (pH 7.5), 1 M NaCl, 20 mM imidazole,  
449 5 mM 2-mercaptoethanol (BME). Cells were lysed using an EmulsiFlex-C5 homogenizer  
450 (Avestin) and lysates were clarified by centrifugation at 30,000 x *g* at 4 °C for 40 min. N  
451 proteins were purified using affinity tag and gel filtration columns. Purity of N proteins  
452 were determined by Coomassie staining of SDS-PAGE. RNA-free species are used for  
453 oligomerization, RNA binding, and ELISA studies.

454  
455 **Negative Staining EM.** 2 μL of N sample at a concentration of 1 mg/mL was applied to  
456 a glow-discharged copper grid (Ted Pella), washed twice with water before staining with  
457 2% uranyl acetate for 30 s, and air dried. Grids were imaged using a JEOL JEM-  
458 1400plus Transmission Electron Microscope operating at 120 kV and recorded with an  
459 AMT XR111 high-speed 4k x 2k pixel phosphor-scintillated 12-bit CCD camera.

460

461 **Dynamic Light Scattering (DLS).** DLS experiments were performed on a DynaPro-  
462 PlateReader II (Wyatt Technologies Corporation). Measurements of N samples in  
463 triplicates (1 mg/mL) were obtained at 25 °C and analyzed using Dynamics software  
464 (Wyatt).

465  
466 **Fluorescence Polarization Assay (FPA).** FPA experiments were performed on a  
467 Cytation5 plate reader (BioTek) operating on Gen5 software. Excitation and emission  
468 wavelengths were set to 485 and 528 nm, respectively, with a bandpass of 20 nm. Read  
469 height and G factor were set to 8.5 mm and 1.26, respectively using the autogain  
470 function. For RNA binding experiments, fluorescein isothiocyanate (FITC) labelled 20-nt  
471 ssRNA or 19-nt siRNA at a final concentration of 1 nM was loaded on N samples (in 20  
472 mM HEPES (pH 7.5), 150 mM NaCl, 2 mM TCEP, 5% glycerol) at concentrations  
473 ranging from 0.4 nM to 10 µM in a 96-well plate. After 10 min of incubation,  
474 fluorescence polarization signals were read. The fluorescence polarization values were  
475 then plotted against N concentrations to fit the dissociation constant,  $K_D$ , using ORIGIN  
476 software. For anisotropy plots, anisotropy values were converted from polarization  
477 according to previous research (Kozlov et al., 2012).

478  
479 **LC-MS Analysis.** Unless otherwise indicated, all chemical reagents were sourced from  
480 Millipore Sigma and used without further purification. For LC-MS analyses, 30 pmol of  
481 protein in 50 µL of 1:1 solvent mixture of acetonitrile:water with 0.1% formic acid  
482 (CovaChem) was loaded onto a C8 trap (ZORBAX Eclipse XDB C8 column, 2.1 x 15  
483 mm, Agilent), desalted for 3 min by using water/0.1% formic acid at a flow rate of 100  
484 µL/min, and eluted using an 14 minute gradient from 0 to 80% acetonitrile/0.1% formic

485 acid at a flow rate of 100  $\mu\text{L}/\text{min}$ . Samples were analyzed using a Maxis 4G Q-TOF  
486 (Bruker Daltonics). The mass spectrum was extracted guided by the elution peak and  
487 submitted to PMI Intact Mass and searched for M values ranging from 5-50 kDa.

488  
489 **HDX-MS.** N<sub>NTD-LKR S176D/S188D/S206D</sub> was incubated with a 20-nt ssRNA at a 1:1 ratio. After  
490 incubation, 2  $\mu\text{L}$  of 50  $\mu\text{M}$  protein/protein-RNA in PBS (pH 7.4) was diluted 10-fold (v/v)  
491 with labeling buffer (PBS in D<sub>2</sub>O, pD 7.0) (D<sub>2</sub>O from Cambridge Isotope Laboratories),  
492 incubated for 10, 30, 300, and 3600 s on ice, quenched by using a 60% dilution with 3  
493 M urea, PBS (pH 2.5), and flash frozen for later LC-MS analysis. A 0 s control was  
494 prepared with PBS in H<sub>2</sub>O. Prior to incubation, each 50  $\mu\text{L}$  of 2  $\mu\text{M}$  sample was thawed  
495 for 1 min at 37 °C before injection into a custom-built liquid chromatography (LC)  
496 apparatus for LC-MS analysis. The labelled protein passed through two in-house  
497 packed protease columns (2 mm x 20 mm), coupled so that the first using protease from  
498 *Aspergillus saitoi* type XIII (FXIII) and the second porcine pepsin (0.1% formic acid, flow  
499 rate 200  $\mu\text{L}/\text{min}$ ); the resulting peptides were trapped on a ZORBAX Eclipse XDB C8  
500 column (2.1 mm x 15 mm, Agilent), desalted for 3 min, and then separated on a  
501 XSelect CSH C18 XP column (130Å, 2.5  $\mu\text{m}$ , 2.1 mm X 50 mm, Waters) with a 10.5 min  
502 linear gradient from 4 – 40% acetonitrile/0.1% formic acid (flow rate 100  $\mu\text{L}/\text{min}$ ). All  
503 valves, tubes, and columns (except for the protease columns, which lose activity at low  
504 temperature) were submerged in ice during the experiment to minimize back exchange.  
505 Peptides were eluted into a Bruker Maxis HM Q-TOF MS for mass analysis.  
506 Experiments were in duplicate unless otherwise indicated. The HDX data processing  
507 was performed by using HDEaminer (version 2.5.1, Sierra Analytics, Inc.).

508  
509 **IFN $\beta$  promoter reporter gene assay.** HEK-293T cells ( $5 \times 10^4$ ) were co-transfected  
510 using Lipofectamine 2000 with 25 ng of an IFN $\beta$  promoter-firefly luciferase reporter  
511 plasmid, 25 ng of pRL-TK *Renilla* luciferase reporter plasmid, and 125, 12.5, and 1.25  
512 ng of the indicated viral protein expression plasmid. Twenty-four hours post-transfection,  
513 cells were mock-treated or SeV (15 hemagglutination units / ml) infected. Eighteen  
514 hours post-treatment or post-infection, cells were lysed and analyzed for luciferase  
515 activity using a Dual-Luciferase reporter assay system (Promega). Firefly luciferase  
516 activity was normalized to *Renilla* luciferase activity. Assays were performed in triplicate;  
517 error bars indicate the standard error of the mean (SEM) for the triplicate. Viral protein  
518 expression was confirmed by Western blot analysis.

519

## 520 **QUANTIFICATION AND STATISTICAL ANALYSIS**

521 All HDX samples for each time point were prepared and acquired in duplicate. HDX  
522 results for peptides with m/z peaks interfering/overlapping with the theoretical centroid  
523 fit were excluded from the analysis. Error bars in the kinetic plots show the standard  
524 deviation for each protein state and time point. Error bars shown in the Woods' plot are  
525 3 times the propagated error for each peptide across all time points (if the error bar  
526 does not cross zero then the difference is potentially significant). The global significance  
527 limit (i.e. the minimum difference in number of deuterium for a statistically significant  
528 difference) is shown in gray. Briefly, we first calculated the pooled standard deviation for  
529 each state, using standard deviations for all peptides and all time points ( $n = 214$   
530 peptides  $\times$  4 states = 856 total data points for each state). From the pooled standard  
531 deviations of each state, the standard error of the mean was calculated for the entire

532 dataset ( $n = 2$  replicates). The global significance limit is then the confidence interval  
533 using this standard error of the mean a t-values for a two-tailed Student's t-distribution (\*,  
534  $p < 0.1$ ; \*\*,  $p < 0.05$ ; \*\*\*,  $p < 0.01$ , 2 degrees of freedom (2 states + 2 replicates – 2)). In  
535 the Woods' plot, peptide HDX differences are considered significant if the difference  
536 exceeds this limit. Peptides are only considered statistically significant if both the  
537 conditions for the propagated error and the global significance limit are met.

538  
539 For ELISA data, the cut-off is represented by the dotted line and calculated as the mean  
540 + 3 standard deviations of the negative population, used to calculate sensitivity and  
541 specificity. Experiments were repeated twice. Statistical significance was calculated by  
542 unpaired Student's t-test using GraphPad Prism.

543  
544 For IFN- $\beta$  promoter assay, statistical significance was determined by performing a one-  
545 way ANOVA followed with Tukey multiple comparison as compared to Sendai virus-  
546 infected control using GraphPad Prism.

547  
548 **Acknowledgements**

549 We thank Dr. N. Krogan (UCSF) for sharing SARS-CoV-2 plasmids, Drs. A. Holehouse  
550 and A. Soranno (Washington University School of Medicine) for providing critical  
551 feedback, and R. Ridings for coordinating studies between WUSM and external groups.  
552 We would like to thank Bruker for mass spectrometry technical and instrument support,  
553 and Protein Metrics (R42GM1213302 to H.W.R) and Sierra Analytics for providing  
554 proteomic and HDX data analysis software. Research was supported by Fast Grant  
555 ##2161 (Emergent Ventures) to G.K.A., by Fast Grant Fast Grants Award # 2158 to

556 C.F.B, and NIH grants (P01AI120943, R01AI123926 to G.K.A. and C.F.B; R01AI107056  
557 to D.W.L.; P41GM103422 and R24GM136766 to M.L.G.; R01AI143292  
558 and R01AI148663 C.F.B). S.A.V was supported by COVID190115 and COVID190126  
559 Health and Medical Research Fund, Food and Health Bureau, Hong Kong and  
560 NIH/NIAID CEIRS contract HHSN272201400006C. A.J.Q. is supported by a NIH T32  
561 training grant (T32CA009547).

562 **Author contributions:** CW, GKA, and DWL conceived the overall project. All authors  
563 were integral to the design and execution of the study. CW, AQ, GKA, and DWL wrote  
564 the initial draft with significant input from all authors.

#### 565 **Declaration of interests**

566 The authors declare no competing interests.

#### 567 **Inclusion and diversity**

568 We worked to ensure sex balance in the selection of non-human subjects. One or more  
569 of the authors of this paper self-identifies as living with a disability. One or more of the  
570 authors of this paper received support from a program designed to increase minority  
571 representation in science.

572

#### 573 **References**

574 Arragain, B., Reguera, J., Desfosses, A., Gutsche, I., Schoehn, G., and Malet, H. (2019). High resolution  
575 cryo-EM structure of the helical RNA-bound Hantaan virus nucleocapsid reveals its assembly  
576 mechanisms. *eLife* 8, e43075.  
577 Bar-On, Y.M., Flamholz, A., Phillips, R., and Milo, R. (2020). SARS-CoV-2 (COVID-19) by the numbers. *eLife*  
578 9, e57309.

579 Bharat, T.A.M., Noda, T., Riches, J.D., Kraehling, V., Kolesnikova, L., Becker, S., Kawaoka, Y., and Briggs,  
580 J.A.G. (2012). Structural dissection of Ebola virus and its assembly determinants using cryo-electron  
581 tomography. *Proceedings of the National Academy of Sciences* *109*, 4275-4280.

582 Bouhaddou, M., Memon, D., Meyer, B., White, K.M., Rezelj, V.V., Correa Marrero, M., Polacco, B.J.,  
583 Melnyk, J.E., Ulferts, S., Kaake, R.M., *et al.* (2020). The Global Phosphorylation Landscape of SARS-CoV-2  
584 Infection. *Cell* *182*, 685-712.e619.

585 Busmann, B.M., Reiche, S., Jacob, L.H., Braun, J.M., and Jassoy, C. (2006). Antigenic and cellular  
586 localisation analysis of the severe acute respiratory syndrome coronavirus nucleocapsid protein using  
587 monoclonal antibodies. *Virus Res* *122*, 119-126.

588 Carlson, C.R., Asfaha, J.B., Ghent, C.M., Howard, C.J., Hartooni, N., Safari, M., Frankel, A.D., and Morgan,  
589 D.O. (2020). Phosphoregulation of phase separation by the SARS-CoV-2 N protein suggests a biophysical  
590 basis for its dual functions. *Molecular Cell*.

591 Chang, C.-k., Hou, M.-H., Chang, C.-F., Hsiao, C.-D., and Huang, T.-h. (2014). The SARS coronavirus  
592 nucleocapsid protein – Forms and functions. *Antiviral Research* *103*, 39-50.

593 Chang, C.-K., Hsu, Y.-L., Chang, Y.-H., Chao, F.-A., Wu, M.-C., Huang, Y.-S., Hu, C.-K., and Huang, T.-H.  
594 (2009). Multiple Nucleic Acid Binding Sites and Intrinsic Disorder of Severe Acute Respiratory Syndrome  
595 Coronavirus Nucleocapsid Protein: Implications for Ribonucleocapsid Protein Packaging. *Journal of*  
596 *Virology* *83*, 2255-2264.

597 Chew, K.L., Tan, S.S., Saw, S., Pajarillaga, A., Zaine, S., Khoo, C., Wang, W., Tambyah, P., Jureen, R., and  
598 Sethi, S.K. (2020). Clinical evaluation of serological IgG antibody response on the Abbott Architect for  
599 established SARS-CoV-2 infection. *Clinical Microbiology and Infection* *26*, 1256.e1259-1256.e1211.

600 Cubuk, J., Alston, J.J., Incicco, J.J., Singh, S., Stuchell-Brereton, M.D., Ward, M.D., Zimmerman, M.I.,  
601 Vithani, N., Griffith, D., Wagoner, J.A., *et al.* (2021). The SARS-CoV-2 nucleocapsid protein is dynamic,  
602 disordered, and phase separates with RNA. *Nature Communications* *12*, 1936.

603 Dinesh, D.C., Chalupska, D., Silhan, J., Koutna, E., Nencka, R., Veverka, V., and Boura, E. (2020a).  
604 Structural basis of RNA recognition by the SARS-CoV-2 nucleocapsid phosphoprotein. *PLOS Pathogens* *16*,  
605 e1009100.

606 Dinesh, D.C., Chalupska, D., Silhan, J., Veverka, V., and Boura, E. (2020b). Structural basis of RNA  
607 recognition by the SARS-CoV-2 nucleocapsid phosphoprotein. *bioRxiv*, 2020.2004.2002.022194.

608 Ding, B., Qin, Y., and Chen, M. (2016). Nucleocapsid proteins: roles beyond viral RNA packaging. *Wiley*  
609 *Interdiscip Rev RNA* *7*, 213-226.

610 Fung, T.S., and Liu, D.X. (2019). Human Coronavirus: Host-Pathogen Interaction. *Annual Review of*  
611 *Microbiology* *73*, 529-557.

612 Grosseohme, N.E., Li, L., Keane, S.C., Liu, P., Dann, C.E., Leibowitz, J.L., and Giedroc, D.P. (2009).  
613 Coronavirus N Protein N-Terminal Domain (NTD) Specifically Binds the Transcriptional Regulatory  
614 Sequence (TRS) and Melts TRS-cTRS RNA Duplexes. *Journal of Molecular Biology* *394*, 544-557.

615 Gui, M., Liu, X., Guo, D., Zhang, Z., Yin, C.-C., Chen, Y., and Xiang, Y. (2017). Electron microscopy studies  
616 of the coronavirus ribonucleoprotein complex. *Protein & Cell* *8*, 219-224.

617 Hachim, A., Kavian, N., Cohen, C.A., Chin, A.W.H., Chu, D.K.W., Mok, C.K.P., Tsang, O.T.Y., Yeung, Y.C.,  
618 Perera, R.A.P.M., Poon, L.L.M., *et al.* (2020). ORF8 and ORF3b antibodies are accurate serological  
619 markers of early and late SARS-CoV-2 infection. *Nature Immunology* *21*, 1293-1301.

620 Iserman, C., Roden, C., Boerneke, M., Sealfon, R., McLaughlin, G., Jungreis, I., Park, C., Boppana, A.,  
621 Fritch, E., Hou, Y.J., *et al.* (2020). Specific viral RNA drives the SARS CoV-2 nucleocapsid to phase  
622 separate. *bioRxiv*, 2020.2006.2011.147199.

623 Jack, A., Ferro, L.S., Trnka, M.J., Wehri, E., Nadgir, A., Costa, K., Schaletzky, J., and Yildiz, A. (2020). SARS  
624 CoV-2 nucleocapsid protein forms condensates with viral genomic RNA. *bioRxiv*,  
625 2020.2009.2014.295824.

- 626 Kang, S., Yang, M., Hong, Z., Zhang, L., Huang, Z., Chen, X., He, S., Zhou, Z., Zhou, Z., Chen, Q., *et al.*  
627 (2020). Crystal structure of SARS-CoV-2 nucleocapsid protein RNA binding domain reveals potential  
628 unique drug targeting sites. *Acta Pharmaceutica Sinica B* *10*, 1228-1238.
- 629 Keane, S.C., Liu, P., Leibowitz, J.L., and Giedroc, D.P. (2012). Functional Transcriptional Regulatory  
630 Sequence (TRS) RNA Binding and Helix Destabilizing Determinants of Murine Hepatitis Virus (MHV)  
631 Nucleocapsid (N) Protein. *Journal of Biological Chemistry* *287*, 7063-7073.
- 632 Kim, D., Lee, J.-Y., Yang, J.-S., Kim, J.W., Kim, V.N., and Chang, H. (2020). The Architecture of SARS-CoV-2  
633 Transcriptome. *Cell* *181*, 914-921.e910.
- 634 Kozlov, A.G., Galletto, R., and Lohman, T.M. (2012). SSB–DNA Binding Monitored by Fluorescence  
635 Intensity and Anisotropy. In *Single-Stranded DNA Binding Proteins: Methods and Protocols*, J.L. Keck, ed.  
636 (Totowa, NJ: Humana Press), pp. 55-83.
- 637 Le Bert, N., Tan, A.T., Kunasegaran, K., Tham, C.Y.L., Hafezi, M., Chia, A., Chng, M.H.Y., Lin, M., Tan, N.,  
638 Linster, M., *et al.* (2020). SARS-CoV-2-specific T cell immunity in cases of COVID-19 and SARS, and  
639 uninfected controls. *Nature* *584*, 457-462.
- 640 Leung, D.W., and Amarasinghe, G.K. (2016). When your cap matters: structural insights into self vs non-  
641 self recognition of 5' RNA by immunomodulatory host proteins. *Curr Opin Struct Biol* *36*, 133-141.
- 642 Liang, Y., Wan, Y., Qiu, L.-w., Zhou, J., Ni, B., Guo, B., Zou, Q., Zou, L., Zhou, W., Jia, Z., *et al.* (2005).  
643 Comprehensive Antibody Epitope Mapping of the Nucleocapsid Protein of Severe Acute Respiratory  
644 Syndrome (SARS) Coronavirus: Insight into the Humoral Immunity of SARS. *Clinical Chemistry* *51*, 1382-  
645 1396.
- 646 Lin, S.-Y., Liu, C.-L., Chang, Y.-M., Zhao, J., Perlman, S., and Hou, M.-H. (2014). Structural Basis for the  
647 Identification of the N-Terminal Domain of Coronavirus Nucleocapsid Protein as an Antiviral Target.  
648 *Journal of Medicinal Chemistry* *57*, 2247-2257.
- 649 Liu, W., Liu, L., Kou, G., Zheng, Y., Ding, Y., Ni, W., Wang, Q., Tan, L., Wu, W., Tang, S., *et al.* (2020).  
650 Evaluation of Nucleocapsid and Spike Protein-Based Enzyme-Linked Immunosorbent Assays for  
651 Detecting Antibodies against SARS-CoV-2. *Journal of Clinical Microbiology* *58*, e00461-00420.
- 652 Lu, S., Xie, X.-x., Zhao, L., Wang, B., Zhu, J., Yang, T.-r., Yang, G.-w., Ji, M., Lv, C.-p., Xue, J., *et al.* (2021).  
653 The immunodominant and neutralization linear epitopes for SARS-CoV-2. *Cell Reports* *34*, 108666.
- 654 Lu, S., Ye, Q., Singh, D., Villa, E., Cleveland, D.W., and Corbett, K.D. (2020). The SARS-CoV-2 Nucleocapsid  
655 phosphoprotein forms mutually exclusive condensates with RNA and the membrane-associated M  
656 protein. *bioRxiv*, 2020.2007.2030.228023.
- 657 Luo, H., Ye, F., Chen, K., Shen, X., and Jiang, H. (2005). SR-Rich Motif Plays a Pivotal Role in Recombinant  
658 SARS Coronavirus Nucleocapsid Protein Multimerization. *Biochemistry* *44*, 15351-15358.
- 659 Luo, M., Terrell, J.R., and Mcmanus, S.A. (2020). Nucleocapsid Structure of Negative Strand RNA Virus.  
660 *Viruses* *12*, 835.
- 661 Mavrakis, M., Kolesnikova, L., Schoehn, G., Becker, S., and Ruigrok, R.W.H. (2002). Morphology of  
662 Marburg Virus NP–RNA. *Virology* *296*, 300-307.
- 663 McBride, R., Zyl, M.v., and Fielding, B. (2014). The Coronavirus Nucleocapsid Is a Multifunctional Protein.  
664 *Viruses* *6*, 2991-3018.
- 665 Messaoudi, I., Amarasinghe, G.K., and Basler, C.F. (2015). Filovirus pathogenesis and immune evasion:  
666 insights from Ebola virus and Marburg virus. *Nature Reviews Microbiology* *13*, 663-676.
- 667 Patel, A., Lee, Hyun O., Jawerth, L., Maharana, S., Jahnke, M., Hein, Marco Y., Stoykov, S., Mahamid, J.,  
668 Saha, S., Franzmann, Titus M., *et al.* (2015). A Liquid-to-Solid Phase Transition of the ALS Protein FUS  
669 Accelerated by Disease Mutation. *Cell* *162*, 1066-1077.
- 670 Perlman, S., and Netland, J. (2009). Coronaviruses post-SARS: update on replication and pathogenesis.  
671 *Nature Reviews Microbiology* *7*, 439-450.

- 672 Raymond, D.D., Piper, M.E., Gerrard, S.R., and Smith, J.L. (2010). Structure of the Rift Valley fever virus  
673 nucleocapsid protein reveals another architecture for RNA encapsidation. *Proceedings of the National*  
674 *Academy of Sciences* *107*, 11769-11774.
- 675 Savastano, A., Ibáñez de Opakua, A., Rankovic, M., and Zweckstetter, M. (2020). Nucleocapsid protein of  
676 SARS-CoV-2 phase separates into RNA-rich polymerase-containing condensates. *Nature*  
677 *Communications* *11*, 6041.
- 678 Sola, I., Almazán, F., Zúñiga, S., and Enjuanes, L. (2015). Continuous and Discontinuous RNA Synthesis in  
679 Coronaviruses. *Annual Review of Virology* *2*, 265-288.
- 680 Su, Z., Wu, C., Shi, L., Luthra, P., Pintilie, G.D., Johnson, B., Porter, J.R., Ge, P., Chen, M., Liu, G., *et al.*  
681 (2018). Electron Cryo-microscopy Structure of Ebola Virus Nucleoprotein Reveals a Mechanism for  
682 Nucleocapsid-like Assembly. *Cell* *172*, 966-978.e912.
- 683 Takeda, M., Chang, C.-k., Ikeya, T., Güntert, P., Chang, Y.-h., Hsu, Y.-l., Huang, T.-h., and Kainosho, M.  
684 (2008). Solution Structure of the C-terminal Dimerization Domain of SARS Coronavirus Nucleocapsid  
685 Protein Solved by the SAIL-NMR Method. *Journal of Molecular Biology* *380*, 608-622.
- 686 Tang, M.S., Hock, K.G., Logsdon, N.M., Hayes, J.E., Gronowski, A.M., Anderson, N.W., and Farnsworth,  
687 C.W. (2020a). Clinical Performance of the Roche SARS-CoV-2 Serologic Assay. *Clinical Chemistry* *66*,  
688 1107-1109.
- 689 Tang, M.S., Hock, K.G., Logsdon, N.M., Hayes, J.E., Gronowski, A.M., Anderson, N.W., and Farnsworth,  
690 C.W. (2020b). Clinical Performance of Two SARS-CoV-2 Serologic Assays. *Clinical Chemistry* *66*, 1055-  
691 1062.
- 692 Wan, W., Kolesnikova, L., Clarke, M., Koehler, A., Noda, T., Becker, S., and Briggs, J.A.G. (2017). Structure  
693 and assembly of the Ebola virus nucleocapsid. *Nature* *551*, 394-397.
- 694 Williams, C.G., Gibbons, J.S., Keiffer, T.R., Luthra, P., Edwards, M.R., and Basler, C.F. (2020). Impact of  
695 Měnglà Virus Proteins on Human and Bat Innate Immune Pathways. *Journal of Virology* *94*, e00191-  
696 00120.
- 697 Wu, C.-H., Chen, P.-J., and Yeh, S.-H. (2014). Nucleocapsid Phosphorylation and RNA Helicase DDX1  
698 Recruitment Enables Coronavirus Transition from Discontinuous to Continuous Transcription. *Cell Host*  
699 *& Microbe* *16*, 462-472.
- 700 Wu, C.-H., Yeh, S.-H., Tsay, Y.-G., Shieh, Y.-H., Kao, C.-L., Chen, Y.-S., Wang, S.-H., Kuo, T.-J., Chen, D.-S.,  
701 and Chen, P.-J. (2009). Glycogen Synthase Kinase-3 Regulates the Phosphorylation of Severe Acute  
702 Respiratory Syndrome Coronavirus Nucleocapsid Protein and Viral Replication. *Journal of Biological*  
703 *Chemistry* *284*, 5229-5239.
- 704 Ye, Q., West, A.M.V., Silletti, S., and Corbett, K.D. (2020). Architecture and self-assembly of the SARS-  
705 CoV-2 nucleocapsid protein. *Protein Science* *29*, 1890-1901.

706

## 707 **Figure legends**

### 708 **Figure 1. Characterization of N oligomerization with dynamic light scattering. A.**

709 Domain architecture of N. N has two structural domains: NTD and CTD. The sequence  
710 between NTD and CTD is a linker region (LKR) containing a serine-arginine rich motif.

711 The Narm, LKR, and Carm are predicted to be disordered based upon sequence

712 analysis. **B.** Sequence identity between N of SARS-CoV-2 and common cold  
 713 coronaviruses and other epidemic severe coronaviruses MERS-CoV and SARS-CoV. **C.**  
 714 Measurements of N oligomerization with dynamic light scattering. Measured  
 715 hydrodynamic radii,  $R_h$ , are reported in D. **D.** Table summarizes the DLS data for all  
 716 constructs. Numbers are reported as average and standard deviation of three  
 717 experiments. See also Figure S1 and S2.

718

719 **Figure 2. SARS-CoV-2 nucleocapsid protein binds RNA with high affinity. A.**

720 Principles of fluorescence polarization assay to measure RNA binding. Increasing  
 721 concentrations of N was titrated into 1 nM of FITC-labeled RNA. Protein binding to  
 722 FITC-RNA leads to slower tumbling of FITC-RNA, resulting in increased fluorescence  
 723 polarization. **B.** Fluorescence polarization binding curves of N constructs to a 20-nt  
 724 ssRNA. The fitted  $K_D$  values are  $0.007 \pm 0.001 \mu\text{M}$  ( $N_{WT}$ , black square),  $16 \pm 12 \mu\text{M}$   
 725 ( $N_{NTD}$ , red circle),  $13 \pm 5 \mu\text{M}$  ( $N_{CTD}$ , blue up triangle),  $0.006 \pm 0.002 \mu\text{M}$  ( $N_{NTD-LKR-CTD}$ ,  
 726 magenta down triangle), and  $0.006 \pm 0.002 \mu\text{M}$  ( $N_{NTD-LKR-CTD-Carm}$ , green diamond). **C.**

727 Fluorescence polarization binding curves of N constructs to a 20-nt ssRNA. The fitted  
 728  $K_D$  values are  $0.006 \pm 0.002 \text{ nM}$  ( $N_{NTD-LKR-CTD}$ , magenta down triangle),  $13 \pm 5 \mu\text{M}$  ( $N_{CTD}$ ,  
 729 blue circle),  $0.50 \pm 0.08 \mu\text{M}$  ( $N_{NTD-LKR}$ , orange star), and  $0.44 \pm 0.04 \mu\text{M}$  ( $N_{NTD-LKR} + N_{CTD}$ ,  
 730 purple pentagon). **D.** Fluorescence polarization binding curves of N constructs to a 20-nt  
 731 ssRNA. The fitted  $K_D$  values are  $0.006 \pm 0.002 \mu\text{M}$  ( $N_{NTD-LKR-CTD}$ , magenta down  
 732 triangle),  $16 \pm 12 \mu\text{M}$  ( $N_{NTD}$ , red circle),  $0.35 \pm 0.04 \mu\text{M}$  ( $N_{LKR-CTD}$ , orange up triangle),  
 733 and  $0.72 \pm 0.09 \mu\text{M}$  ( $N_{NTD} + N_{LKR-CTD}$ , purple down triangle). **E.** Fluorescence  
 734 polarization binding curves of N constructs to a siRNA. The fitted  $K_D$  values are  $0.051 \pm$

735 0.004  $\mu\text{M}$  ( $N_{\text{WT}}$ , black square),  $124 \pm 84 \mu\text{M}$  ( $N_{\text{NTD}}$ , red circle),  $65 \pm 44 \mu\text{M}$  ( $N_{\text{CTD}}$ , blue  
736 up triangle),  $2.5 \pm 0.5 \mu\text{M}$  ( $N_{\text{NTD-LKR}}$ , magenta down triangle),  $0.22 \pm 0.02 \mu\text{M}$  ( $N_{\text{NTD-LKR-}}$   
737  $\text{CTD}$ , green diamond), and  $0.10 \pm 0.01 \mu\text{M}$  ( $N_{\text{NTD-LKR-CTD-Carm}}$ , navy left triangle). **F.** Table  
738 summarizes  $K_D$  values ( $\mu\text{M}$ ) for key constructs binding to ssRNA and siRNA. Numbers  
739 are reported as average and standard deviation of two experiments. See also Figure S3.

740

741 **Figure 3. HDX-MS mapping of RNA binding to  $N_{\text{NTD-LKR S176D/S188D/S206D}}$ .** **A.** Woods'  
742 plot showing cumulative differential HDX and validating differences using global  
743 significance limits. The horizontal bars depict the cumulative HDX differences between  
744 the RNA-bound and unbound  $N_{\text{NTD-LKR S176D/S188D/S206D}}$ . Standard deviations are shown  
745 for each peptide. Peptides showing statistically significant differences are differentiated  
746 by global significance limit using this standard error of the mean a t-values for a two-  
747 tailed Student's t-distribution (\*,  $p < 0.1$ ; \*\*,  $p < 0.05$ ; \*\*\*,  $p < 0.01$ ). The blue shade of  
748 the peptide bar indicates differing statistical significance (light blue, medium blue, and  
749 navy, respectively); gray peptide bars depict peptides where statistically significant  
750 differences in HDX were not observed. Vertical bars show previously reported binding  
751 sites (residues reported for RNA-binding CoV2 N-protein (Dinesh et al., 2020b; Ye et al.,  
752 2020), AMP-binding HCoV-OC43 (Lin et al., 2014; Ye et al., 2020), and for both are  
753 shown in red, yellow, and orange, respectively). Secondary structure (PDB 6M3M) is  
754 shown above. **B.** Representative kinetic plots showing peptide level HDX as a function  
755 of exchange time (unbound, black; bound to RNA, red). **C.** Sites of protection measured  
756 by HDX mapped on the  $N_{\text{NTD}}$  structure (PDB 6M3M). Statistically significant HDX  
757 protection, regions of no difference in HDX, and regions where lacking proteolytic

758 coverage results in no data are shown in teal, light gray, and dark gray, respectively.  
759 Those residues unresolved in the structure are shown as a dashed line, with the  
760 exception of those reporting a statistically significant difference in teal. **D.** Electrostatic  
761 potential calculated with APBS mapped on to the N<sub>NTD</sub> structure (PDB 6M3M) shows a  
762 major positive charge groove. Red and blue represent negative and positive  
763 electrostatic potential. The color scale is in  $kTe^{-1}$  units. See also Figure S4 and  
764 Mendeley dataset (doi:10.17632/sv8r6phkzt.1).

765

766 **Figure 4. N-RNA forms liquid droplets and phosphorylation modulates N-RNA**  
767 **interactions. A.** Size exclusion chromatography of N constructs (N<sub>WT</sub>, black; N<sub>NTD-LKR-</sub>  
768 CTD-C<sub>arm</sub>, red; N<sub>NTD-LKR-CTD</sub>, blue) in 25 mM HEPES, 500 mM NaCl, 2 mM TCEP, 5%  
769 glycerol. Samples from peak 1 (p1) and p2 contain RNA whereas p3 are RNA-free  
770 based upon absorbance from the 260/280 ratio. **B.** Negative stain electron microscopy  
771 (EM) image of p1 and p2 for N<sub>WT</sub>, N<sub>NTD-LKR-CTD-C<sub>arm</sub></sub>, and N<sub>NTD-LKR-CTD</sub> in 150 mM NaCl.  
772 Samples were diluted into 150 mM NaCl before negative-staining fixation by uranyl  
773 acetate. **C.** Size exclusion chromatography of N constructs (N<sub>WT</sub>, black; N<sub>S188D/S206D</sub>,  
774 blue; N<sub>S176D/S188D/S206D</sub>, red) in 25 mM HEPES, 500 mM NaCl, 2 mM TCEP, 5% glycerol.  
775 **D.** Negative stain electron microscope image of N<sub>S188D/S206D</sub> and N<sub>S176D/S188D/S206D</sub> in 150  
776 mM NaCl. **E.** Fluorescence polarization binding curves of N mutants to a 20-nt ssRNA.  
777 The fitted  $K_D$  values are  $0.007 \pm 0.001 \mu\text{M}$  (N<sub>WT</sub>, black square),  $0.015 \pm 0.002 \mu\text{M}$   
778 (N<sub>S176D/S188D/S206D</sub>, black circle),  $0.505 \pm 0.075 \mu\text{M}$  (N<sub>NTD-LKR</sub>, orange up triangle), and  $1.1$   
779  $\pm 0.2 \mu\text{M}$  (N<sub>NTD-LKR S176D/S188D/S206D</sub>, orange down triangle). Numbers are reported as  
780 average and standard deviation of two experiments. See also Figure S5.

781

782 **Figure 5. The CTD of N is a highly sensitive serological marker. A.** ELISA data of  
783  $N_{WT}$  screened against plasma of COVID-19 positive and negative individuals from a  
784 combined Hong Kong, PRC and St. Louis, MO, USA cohort. Black solid line indicates  
785 the mean  $OD_{450}$  value for each population. \*\*\*\*  $p < 0.0001$ . **B.** ELISAs with the various  
786 N constructs for patient IgG. ELISAs were performed on plasma samples from COVID-  
787 19 patients ( $n = 68$ ) and negative controls ( $n = 28$ ). The cut-off is represented by the  
788 dotted line and calculated as the mean + 3 standard deviations of the negative  
789 population. Mean values  $\pm$  standard deviation of COVID-19 and negative groups are  
790 shown. **C.** Sensitivity and specificity for each of the N domains calculated from the  
791 ELISA results. **D.** Heat-map of ELISA results for  $N_{NTD-LKR-CTD-Carm}$ ,  $N_{CTD}$ , and  $N_{NTD}$   
792 constructs from COVID-19 samples ( $n = 67$ ). Each column represents an individual  
793 sample. **E.** Maturation of the  $N_{CTD}$  and  $N_{NTD-LKR-CTD-Carm}$  IgG response over time ( $n = 67$ ).  
794 **F.** Ratio of  $OD_{450}$  for  $N_{CTD}$  and  $N_{NTD-LKR-CTD-Carm}$  for acute and convalescent time-points.  
795 Mean values  $\pm$  standard deviation of acute and convalescent COVID-19 samples are  
796 shown. Experiments were repeated twice. Statistical significance was calculated by  
797 unpaired Student's t-test, \*\*\*\* $p < 0.0001$ . **G.** Inhibition of SeV-induced IFN $\beta$  promoter  
798 activation by N constructs. Fold changes are relative to vector-only (V) transfections  
799 without SeV infection. MLAV VP35 served as a positive control for inhibition. Three  
800 transfection concentrations were used: 1.25, 12.5, and 125 ng/well. Statistical  
801 significance was determined by performing a one-way ANOVA followed with Tukey  
802 multiple comparison as compared to Sendai virus-infected control; \*\*\*\*  $p < 0.0001$ , \*\*\*  $p$   
803  $< 0.0002$ , \*\*  $p < 0.0021$ , \*  $p < 0.0332$ .

Journal Pre-proof

**TABLE FOR AUTHOR TO COMPLETE**

Please upload the completed table as a separate document. **Please do not add subheadings to the key resources table.** If you wish to make an entry that does not fall into one of the subheadings below, please contact your handling editor. **Any subheadings not relevant to your study can be skipped.** (NOTE: For authors publishing in Cell Genomics, Cell Reports Medicine, Current Biology, and Med, please note that references within the KRT should be in numbered style rather than Harvard.)

**KEY RESOURCES TABLE**

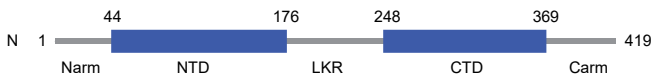
REAGENT or RESOURCE	SOURCE	IDENTIFIER
<b>Antibodies</b>		
Anti-human IgG secondary Ab labeled with HRP	Southern BioTech	Cat#905209
<b>Bacterial and virus strains</b>		
E. coli BL21(DE3)	Agilent	Cat#200131
SeV	Department of Microbiology, Icahn School of Medicine at Mount Sinai, New York, NY USA	N/A
<b>Biological samples</b>		
Human Plasma, Patient with Confirmed SARS-CoV-2 Infection	Barnes-Jewish Hospital, St. Louis, MO, USA	N/A
Human Plasma, Patient with Confirmed SARS-CoV-2 Infection	Hong Kong University and HK Island West Cluster of Hospitals, Hong Kong, PRC	N/A
Human Plasma, Patient with negative test	Barnes-Jewish Hospital, St. Louis, MO, USA	N/A
<b>Chemicals, peptides, and recombinant proteins</b>		
LC-MS grade formic acid	CovaChem	Cat# PI 85171; CAS 64-18-6
Phosphate buffered saline tablets	Millipore Sigma	Cat# P4417
Deuterium oxide (D, 99.9%)	Cambridge Isotope Laboratories	Cat# DLM-4-100; CAS 7789-20-0;
Urea	Millipore Sigma	Cat# U4883; CAS: 57-13-6
2% Uranyl Acetate	Ted Pella	19481
<b>Critical commercial assays</b>		
Dual-Glo luciferase kit	Promega	Cat#E2920
<b>Deposited data</b>		
<b>Experimental models: Cell lines</b>		
Human: HEK293T cells	ATCC	CRL-3216

Experimental models: Organisms/strains		
Oligonucleotides		
20nt ssRNA sequence: UUUCACCUCCCUUUCAGUUU	GenScript	N/A
19nt siRNA sequence: GGAAGAUUAAUAAUUUCC	GenScript	N/A
Recombinant DNA		
Plasmid pET28a-CterTEV His6 SARS-CoV-2 N 1-419	This work	N/A
Plasmid pET28a-CterTEV His6 SARS-CoV-2 N 44-419	This work	N/A
Plasmid pET28a-CterTEV His6 SARS-CoV-2 N 44-369	This work	N/A
Plasmid pET28a-CterTEV His6 SARS-CoV-2 N 44-247	This work	N/A
Plasmid pET28a-CterTEV His6 SARS-CoV-2 N 44-176	This work	N/A
Plasmid pET28a-CterTEV His6 SARS-CoV-2 N 248-369	This work	N/A
Plasmid pCAGGS MLAV VP35	This work	N/A
Plasmid pCAGGS SARS-CoV-2 N 1-419	This work	N/A
Plasmid pCAGGS SARS-CoV-2 N 44-369	This work	N/A
Plasmid pCAGGS SARS-CoV-2 N 44-176	This work	N/A
Plasmid pCAGGS SARS-CoV-2 N 248-419	This work	N/A
Plasmid pCAGGS SARS-CoV-2 N 248-369	This work	N/A
IFN- $\beta$ promoter-firefly luciferase reporter plasmid	Department of Microbiology, Icahn School of Medicine at Mount Sinai, New York, NY USA	N/A
pRL-TK Renilla luciferase reporter plasmid	Promega	E2231
Software and algorithms		
Intact Mass <sup>TM</sup>	Protein Metrics Incorporated	Version 3.11
Byonic <sup>TM</sup>	Protein Metrics Incorporated	Version 3.11
Byologic <sup>TM</sup>	Protein Metrics Incorporated	Version 3.11
DataAnalysis v 4.4	Bruker Daltonics	Version 4.4
HDExaminer	Sierra Analytics Incorporated	Version 2.5.1
Origin	OriginLab	Version 7
UCSF Chimera	Pettersen, <i>et al.</i> , 2004	<a href="http://www.cgl.uscf.edu/chimera/">http://www.cgl.uscf.edu/chimera/</a>
PRISM	GraphPad	Version 7
Dynamics Software	Wyatt	Version 7
Gen5 Software	BioTek	Version 3
Other		
ZORBAX Eclipse XDB C8 trap column (2.1 x 15 mm)	Agilent Technologies	Cat# 975700-936
XSelect CSH C18 XP (130 Å, 2.5 $\mu$ m, 2.1 x 50 mm)	Waters Corporation	Cat# 186006101
MaXis II 4G Q-TOF	Bruker Daltonics	N/A

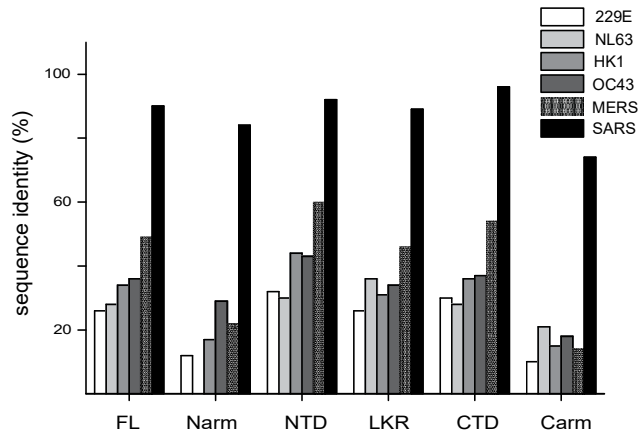
MaXis II HM Q-TOF	Bruker Daltonics	N/A
EmulsiFlex-C5 homogenizer	Avestin	N/A
Glow-Discharged Copper Grid, 200 mesh	Ted Pella	01840-F
JEM-1400 plus TEM	JEOL	N/A
Phosphor-Scintillated 12-bit CCD Camera	AMT	XR111
DynaPro-PlateReader II	Wyatt Technologies Corporation	N/A
Cytation5 Plate Reader	BioTek	N/A

Journal Pre-proof

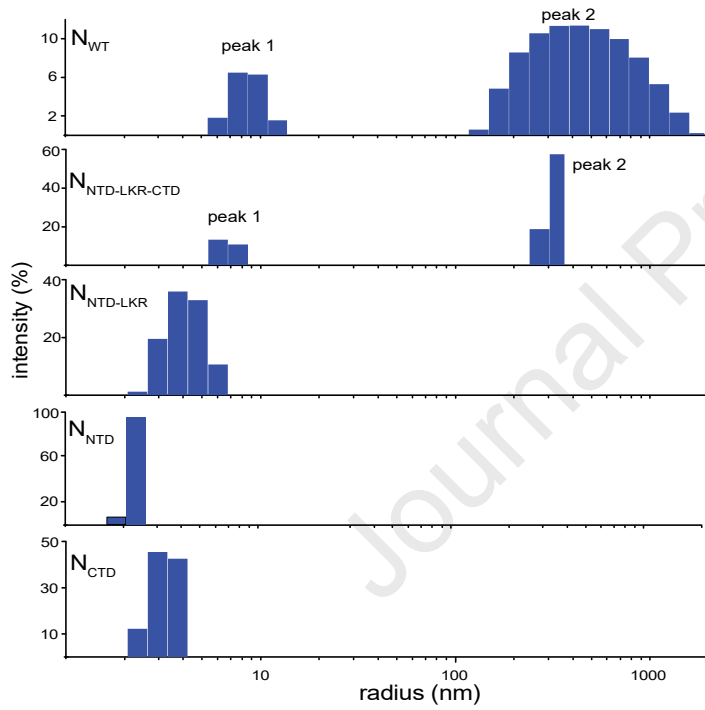
A



B



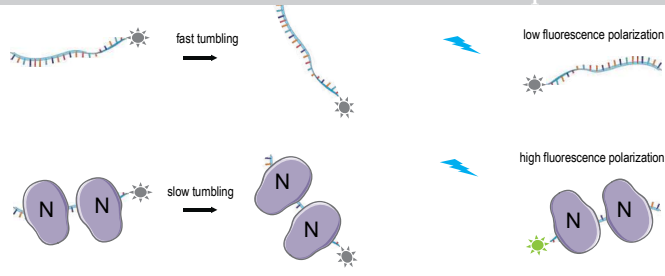
C



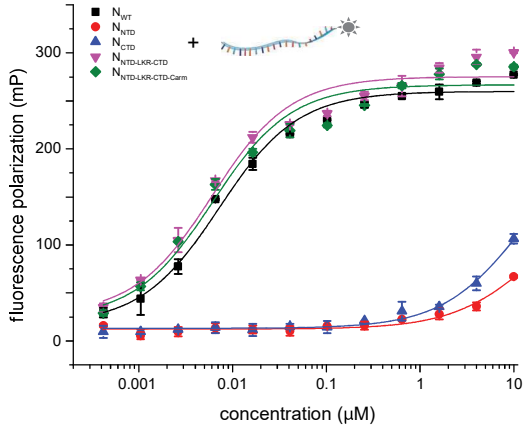
D

	MW (kDa)	Rh (nm)	
		peak 1	peak 2
$N_{WT}$	46	$8.9 \pm 0.2$	$450 \pm 100$
$N_{NTD-LKR-CTD}$	35	$6.5 \pm 0.4$	$360 \pm 20$
$N_{NTD-LKR}$	22	$3.9 \pm 0.1$	
$N_{NTD}$	14	$2.3 \pm 0.1$	
$N_{CTD}$	14	$3.5 \pm 0.1$	

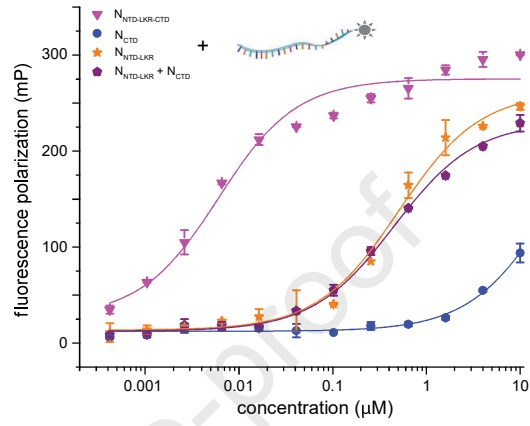
A



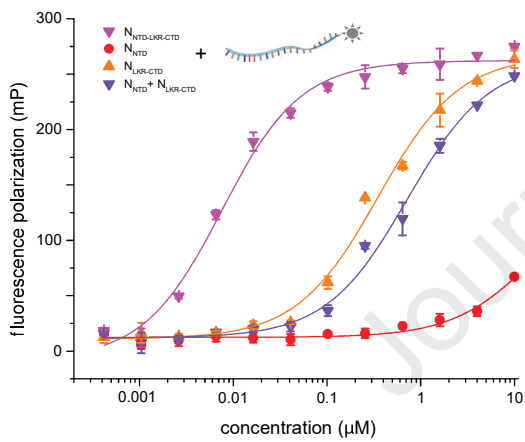
B



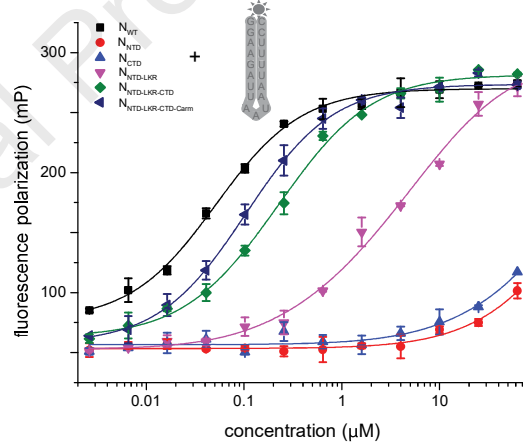
C



D



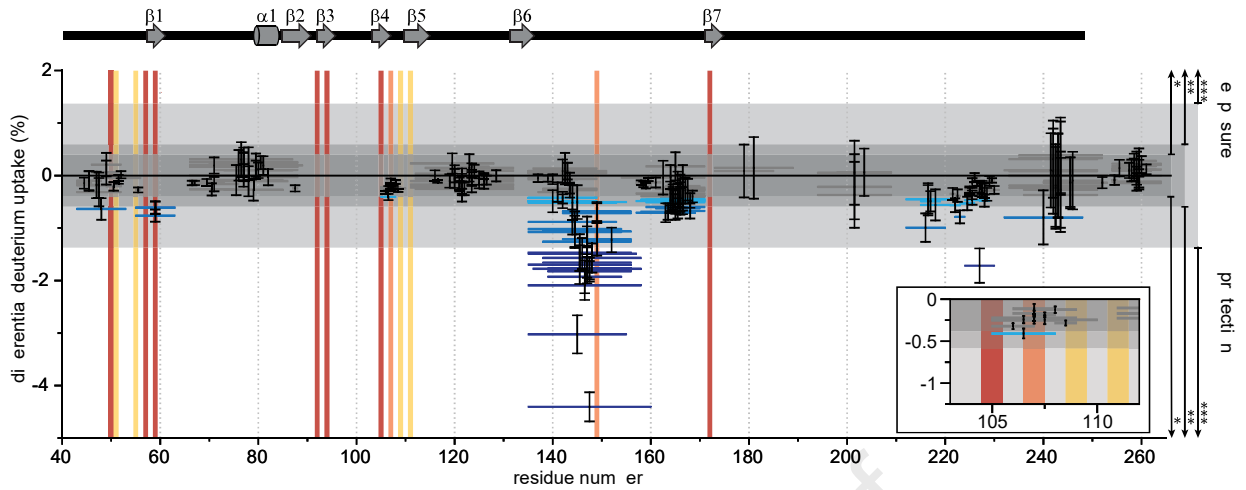
E



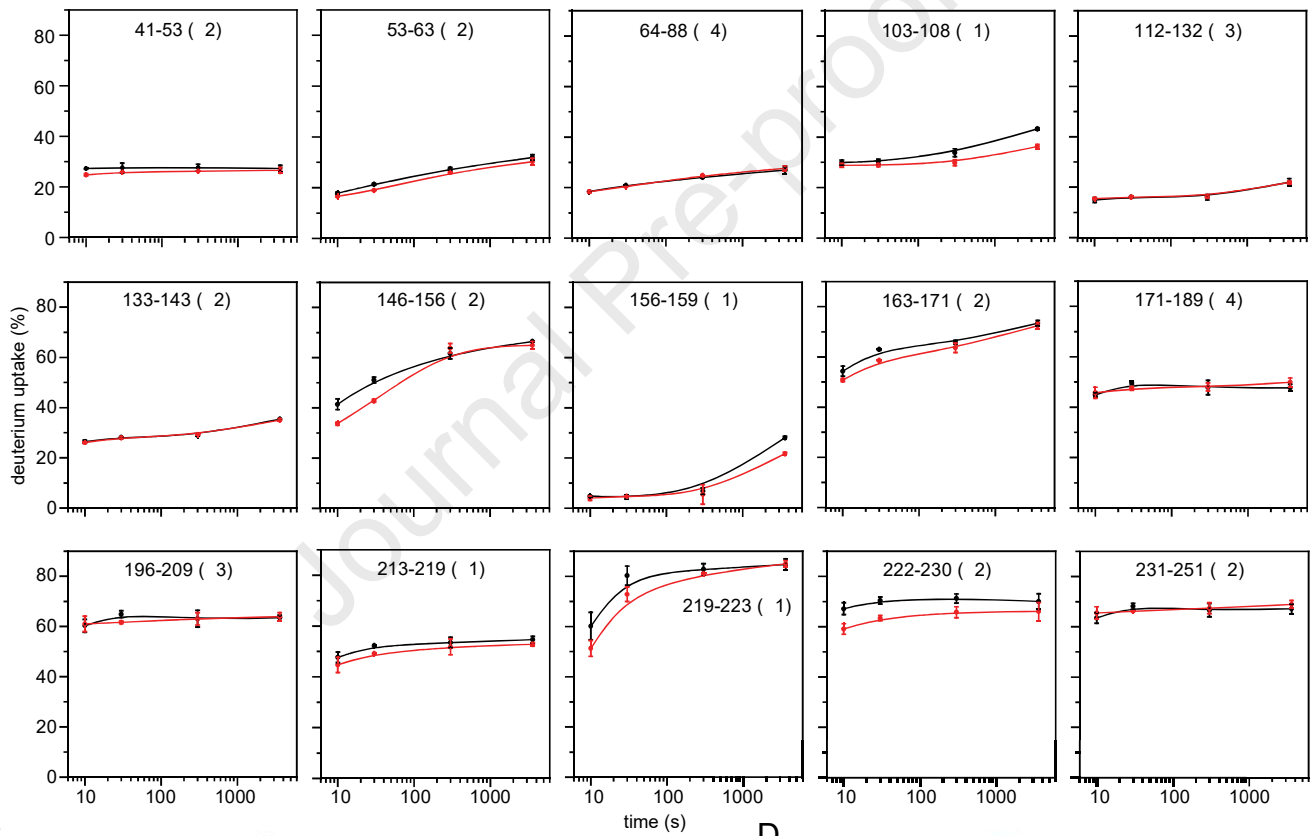
F

	$N_{WT}$	$N_{NTD-LKR-CTD-Carm}$	$N_{NTD-LKR-CTD}$	$N_{NTD-LKR}$	$N_{NTD}$	$N_{CTD}$
	$0.007 \pm 0.001$	$0.006 \pm 0.002$	$0.006 \pm 0.002$	$0.50 \pm 0.08$	$20 \pm 10$	$13 \pm 5$
	$0.051 \pm 0.004$	$0.10 \pm 0.01$	$0.22 \pm 0.02$	$2.5 \pm 0.5$	$120 \pm 80$	$60 \pm 40$

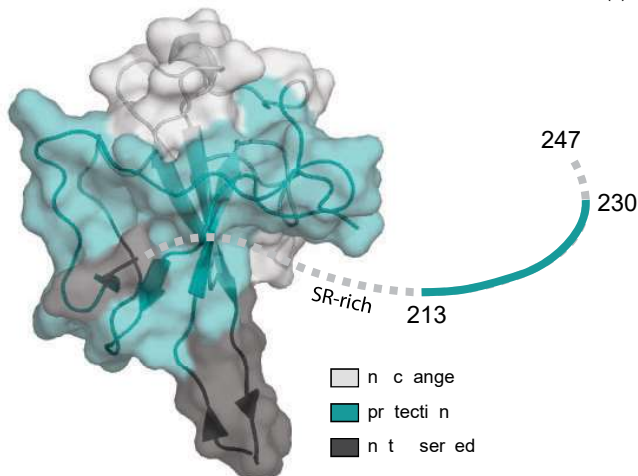
A



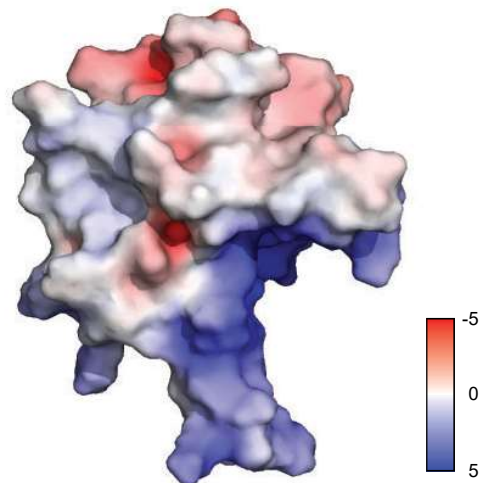
B

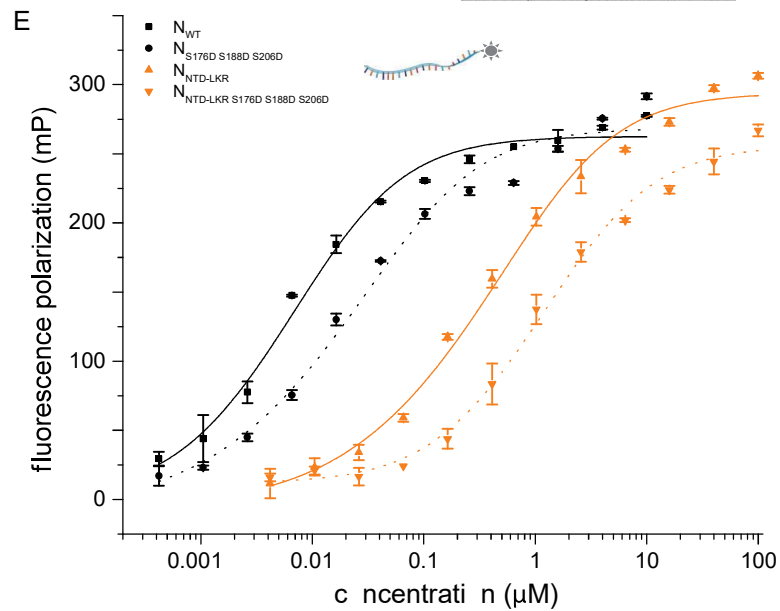
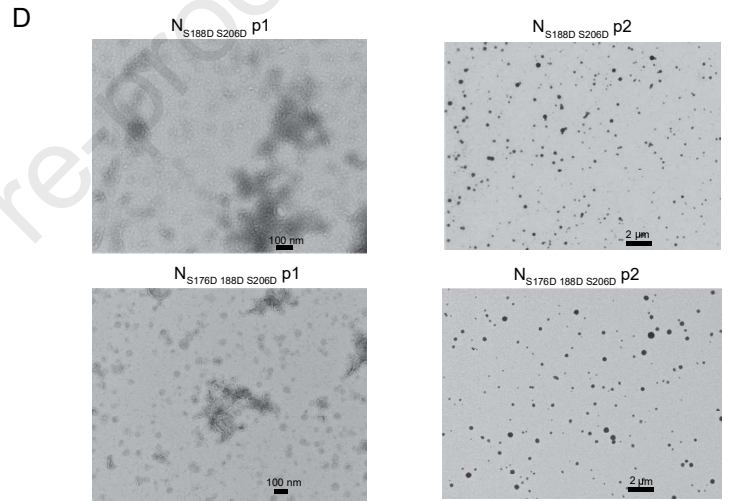
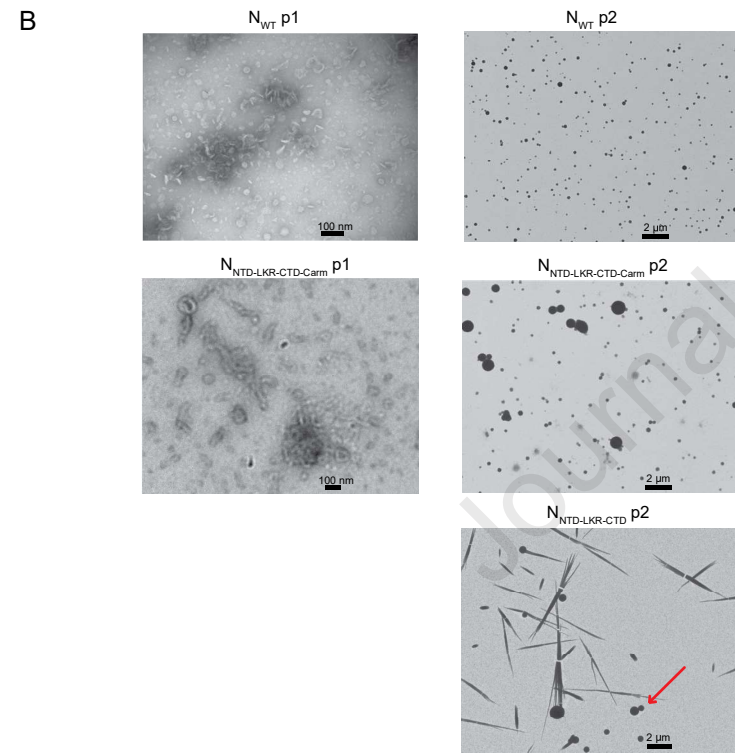
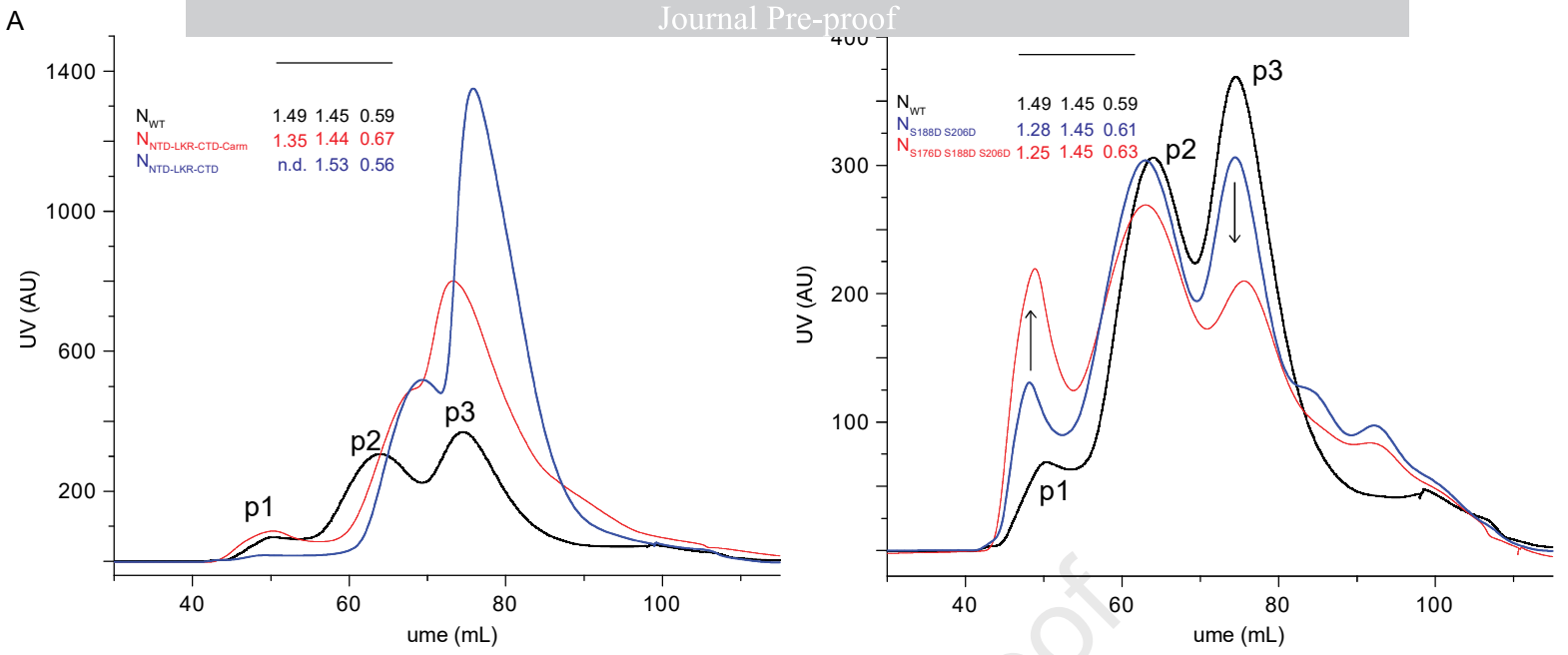


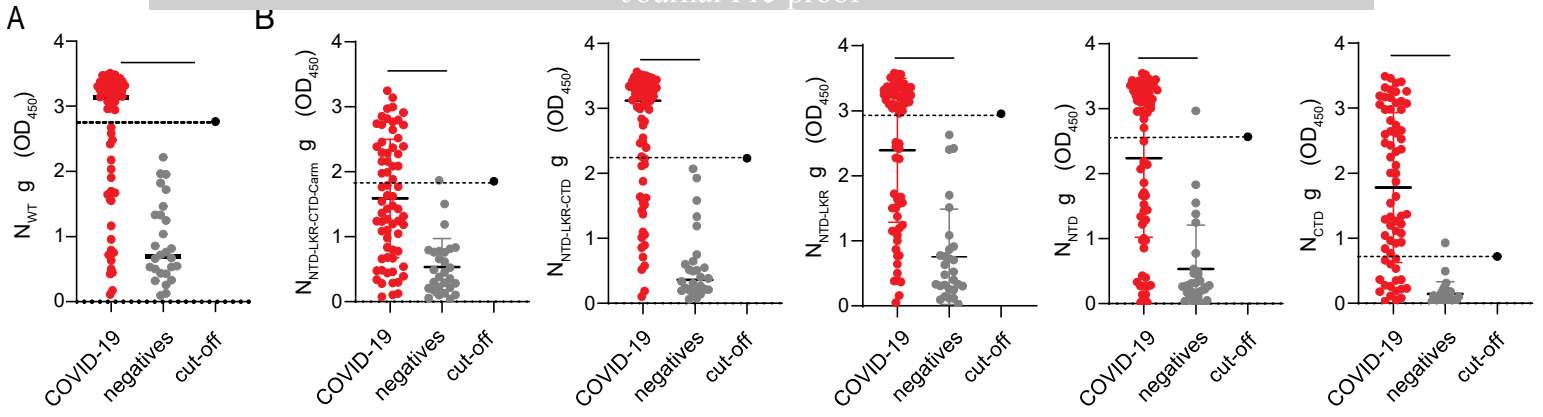
C



D

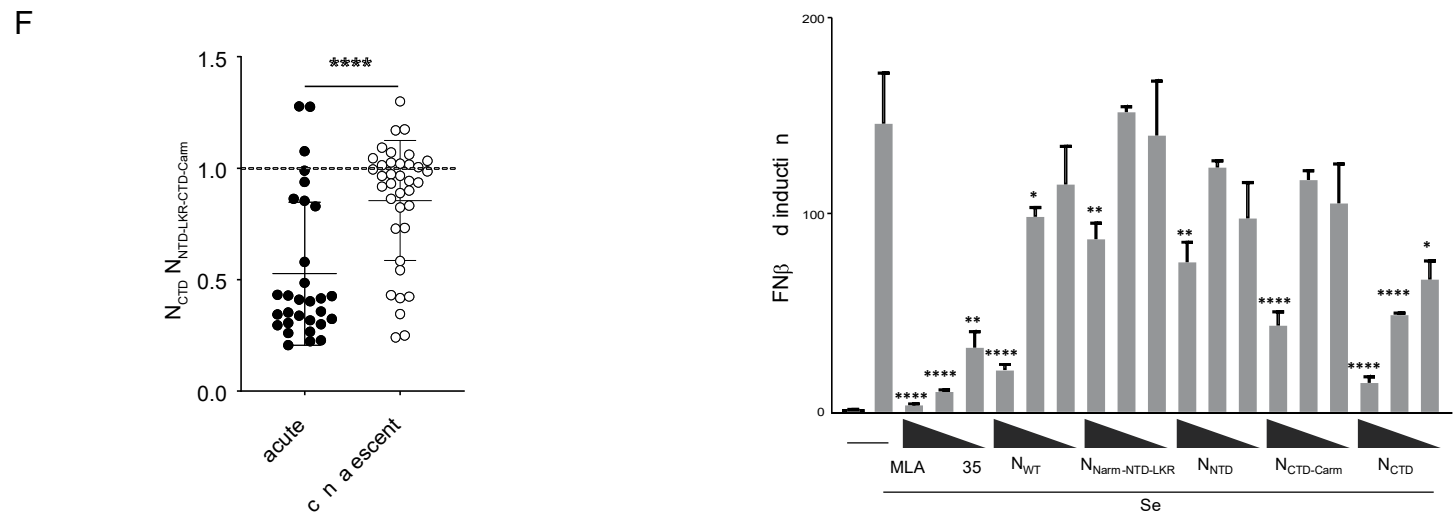
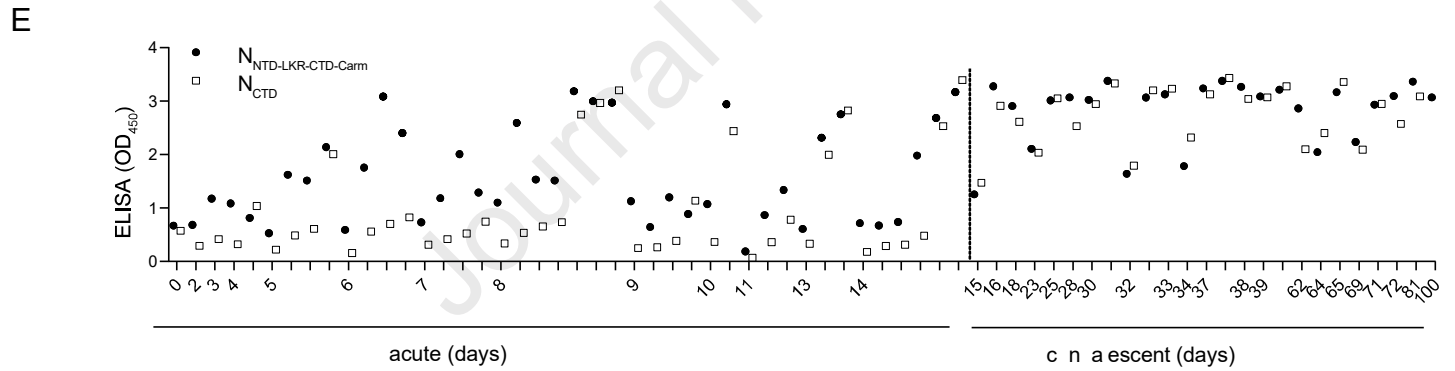
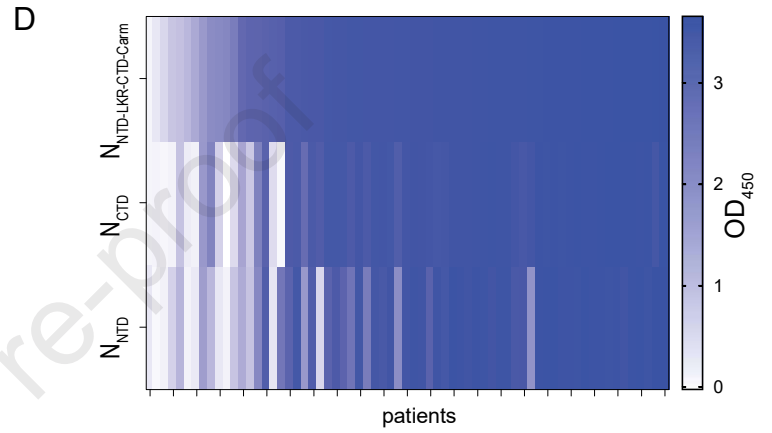






**C**

	sensitivity (%)	specificity (%)
$N_{WT}$	66.2	100
$N_{NTD-LKR-CTD-Carm}$	41.2	96.4
$N_{NTD-LKR-CTD}$	70.6	100
$N_{NTD-LKR}$	54.4	100
$N_{NTD}$	54.4	96.4
$N_{CTD}$	75.0	96.4



- Domain specific contributions of SARS-CoV-2 N to oligomerization and RNA binding.
- Phosphorylation of N modulate RNA binding affinity and N-RNA solution properties.
- HDX-MS results probe RNA binding interface of SARS-CoV-2 N.
- CTD may be a more sensitive and specific serological marker of infection.

Journal Pre-proof